Redox Biology 85 (2025) 103673

Contents lists available at ScienceDirect

Redox Biology

journal homepage: www.elsevier.com/locate/redox

Sestrin2 alleviates cognitive impairment via inhibiting hippocampus ferroptosis in cigarette smoke-induced chronic obstructive pulmonary disease☆

Da-Wei Zhang [a,b,1], Ming-Ming Yang [a,b,1], Meng-Xi Zhou [a,b,1], Yuan-Yuan Wei [a,b], Lei Hu [a,b], Mei Hong [a,b], Ting-Ting Chen [a,b], Xiao-Min Wang [c], Yi-Chuan Ding [a,b], Chuan-Sheng Wei [d,e], Fang Li [a,b], Wen Chen [f], Jia-Ying Kang [a,b], Jing-Jing Ye [a,b], Guang-He Fei [a,b,*]

[a] Department of Respiratory and Critical Care Medicine, First Affiliated Hospital of Anhui Medical University, Hefei, 230022, Anhui Province, People's Republic of China
[b] Key Laboratory of Respiratory Diseases Research and Medical Transformation of Anhui Province, Hefei, 230022, Anhui Province, People's Republic of China
[c] Department of Radiology, First Affiliated Hospital of Anhui Medical University, Hefei, 230022, Anhui Province, People's Republic of China
[d] School of Basic Medical Sciences, Anhui Medical University, Hefei, 230022, Anhui Province, People's Republic of China
[e] Biopharmaceutical Research Institute, Anhui Medical University, Hefei, 230022, Anhui Province, People's Republic of China
[f] Department of Anesthesiology, First Affiliated Hospital of Anhui Medical University, Hefei, 230022, Anhui Province, People's Republic of China

ARTICLE INFO

Keywords:
Sestrin2
Hippocampus
Ferroptosis
Cognitive dysfunction
Chronic obstructive pulmonary disease

ABSTRACT

Cognitive dysfunction is an essential comorbidity that contributing to the whole disease process of the individual of chronic obstructive pulmonary disease (COPD), yet its specific mechanism remains controversial due to a lack of cellular and molecular evidence. Our clinical data revealed a significant reduction in total hippocampal volume in patients with COPD, with the CA1 subfield notably smaller and associated with lung function. Long-term CS exposure caused hippocampus impairment, leading to spatial and working memory impairments in COPD model mice. CS exposure triggered ferroptosis in vivo and in vitro. Bioinformatics analysis suggested that sestrin2 is a key ferroptosis-related gene involved in cognitive impairment. Sestrin2 protein levels were consistently increased in the hippocampus of COPD model mice and CSE treated HT22 cells. Sestrin2 knockdown exacerbated ferroptosis and enhanced the down-regulation of synaptophysin and PSD95, while sestrin2 overexpression inhibited these damaging processes in vitro. This neuroprotection of sestrin2 is dependent on its binding with heterogeneous nuclear ribonucleoprotein L (HNRNPL). Moreover, sestrin2 overexpression and DFO ameliorated hippocampal impairment and neurocognitive deficits by correcting CS-induced ferroptosis and synaptic proteins alterations in vivo. Overall, our study reveals that sestrin2 improves CS-induced adverse changes in hippocampal neurons and neurobehavior, providing new insights into the molecular mechanisms underlying COPD-related cognitive dysfunction.

1. Introduction

Chronic obstructive pulmonary disease (COPD) is a prevalent chronic respiratory disease with a variety of extra-pulmonary manifestations [1]. Up to 61 % of patients with COPD have cognitive impairment [2–4], leading to reduced quality of life, elevated hospitalization rates, and increased mortality [5–7]. The hippocampus, a critical region responsible for cognitive functions, is particularly vulnerable to noxious particles and gases induced-inflammatory damage [8]. Our previous studies have shown that the atrophied hippocampus can be found even in the early stage of COPD [9]. Understanding the molecular and cellular events evoked by COPD is essential for comprehending the adaptive mechanisms and effective therapeutic interventions for COPD-related cognitive dysfunction.

Cigarette smoke (CS) is a significant pathogenic factor in many patients with COPD [10]. The harmful particles present in CS can induce

☆ The authors declare that there are no conflicts of interests.

* Corresponding author. Department of Respiratory and Critical Care Medicine, First Affiliated Hospital of Anhui Medical University, Hefei, 230022, Anhui Province, People's Republic of China.
E-mail address: gh.fei@ahmu.edu.cn (G.-H. Fei).

[1] These authors contributed equally to this work.

https://doi.org/10.1016/j.redox.2025.103673
Received 7 April 2025; Received in revised form 10 May 2025; Accepted 11 May 2025
Available online 13 May 2025
2213-2317/© 2025 The Authors. Published by Elsevier B.V. This is an open access article under the CC BY-NC-ND license (http://creativecommons.org/licenses/by-nc-nd/4.0/).

emphysema and airway changes [11]. Simultaneously, continuous low-grade inflammation and oxidants induced by CS in the lungs can spill over and enter the systemic circulation, exerting toxic effects on neurons and inhibiting the central nervous system [12,13]. Although persistent systemic inflammation resulting from pulmonary inflammation is critical in in the onset of brain-related comorbidity, local neuroinflammatory processes within the brain also significantly contribute to cognitive impairment [14,15]. Cigarettes contain a number of highly water-soluble toxic substances that are absorbed into the bloodstream and then flow to the brain [16], causing neuroinflammatory responses and oxidative damage, ultimately damaging the brain structure and function [17]. Although a recognized association exists between CS exposure and impaired neurocognitive outcomes [18,19], the underlying mechanism remains unclear.

Ferroptosis, a form of cell death characterized by lethal iron-dependent lipid peroxidation, is closely linked to cognitive impairment and COPD occurrence [20,21]. The brain is highly susceptible to CS-induced oxidative stress because of its high metabolism and energy demand [22] and the abundance of polyunsaturated fatty acids susceptible to Reactive oxygen species(ROS) [23]. Kampmann demonstrated that the ferroptosis inhibitor GPX4 is required for neuronal survival under oxidative stress, suggesting that neurons are prone to ferroptosis when exposed to oxidative stress [23]. Jing [24] found that ferroptosis was involved in smoking-related osteoporosis; however, the role of ferroptosis in cognitive impairment associated with COPD has not been well studied.

Sestrin2 is a highly conserved protein that plays a protective role against oxidative stress [25]. Recent studies had confirmed that sestrin2 may regulate ferroptosis through various pathways, including sepsis and intestinal ischemia-reperfusion [26,27]. Our previous research also demonstrated elevated expression of sestrin2 in patients with COPD [28]. Considering the profound impact of sestrin2 on the pathological process of ferroptosis, we designed this study to investigate the regulatory effect of sestrin2 on COPD-related cognitive dysfunction via a long-term CS exposure induced-COPD mouse model in vivo and hippocampal neuronal cell HT22 in vitro. Our findings will help to develop more precise treatment strategies for COPD-related comorbidities, thereby improving the overall prognosis of patients with COPD.

2. Methods

2.1. Subjects

One hundred subjects were included in this study, including 50 patients with COPD and 50 controls. Patients with COPD were diagnosed according to the Global Initiative for Chronic Obstructive Lung Disease guidelines and were in the stable phase for≥12 weeks. The exclusion criteria included the presence of other pulmonary diseases, chronic kidney or liver conditions, dementia, sleep disorders, head injuries, psychiatric disorders (e.g., anxiety disorders, schizophrenia, depression, or alcohol abuse), and the use of any medications that could potentially impact cognitive function [9,29]. This protocol was approved by the Ethics Committee of the First Affiliated Hospital of Anhui Medical University (No. PJ2024-07-58).

2.2. Magnetic resonance imaging (MRI) data acquisition and analysis

Anatomical MRI data were acquired on an MR750w 3.0 TMRI scanner (General Electric, Waukesha, WI, USA) using a 16-channel head coil. A T1-weighted three-dimensional (3D) structure spoiled gradient recalled echo sequence was used for anatomical MRI (repetition time [TR]/echo time [TE]/inversion time: 8.5/3.3/900 ms; matrix: 256 × 256; FOV: 240 × 240 mm; slice thickness: 1.2 mm without intervals; and scanning time: 8 min 59 s). FreeSurfer software (https://surfer.nmr.mgh.harvard.edu) was used to obtain the estimated total intracranial volume (eTIV) and the hippocampal subfield volume in each hemisphere. The hippocampus is divided into 12 subfields, Including CA1, CA2, CA3, CA4, GC-ML-DG, fimbria, molecular layer, hippocampal tail, hippocampal fissure, parasubiculum, HATA, presubiculum, and subiculum.

2.3. Establishment and treatment of the COPD model

All animal experiments were approved by the Ethics Committee of Anhui Medical University (No. LLSC20242226). Male C57BL/6 mice (6–8 weeks old) were divided into control and CS-exposure groups. The control mice were exposed to room air. The CS-exposure mice were exposed to CS (300 mg m^{-3} of total particulate matter) in a whole-body exposure system for 90 min twice a day, 4 h apart,6 days a week for 24 weeks. We also established a COPD model by intranasal instillation of a 100 μl mixture of 7 μg of LPS and 1.2 U of porcine pancreatic ELT once a week for 4 weeks [30]. The control animals received 100 μl of PBS intranasally once a week for 4 weeks. In the pharmacological treatment experiments, DFO was dissolved in ddH_2O. According to previous study, DFO (100 mg/kg) was intraperitoneal injection continuously at 10 a.m. during the CS treatment process(21–24week) [24]. All mice were housed under a 12-h light-dark cycle and had free access to sterilized food and water.

2.4. Measurement of lung function

Mice were intubated and connected to a whole-body plethysmograph of PFT Pulmonary Maneuvers (DSI Buxco, Minnesota, USA). Forced vital capacity (FVC) and forced expiratory volume in 20 ms (FEV20) were recorded within 10 min. To ensure reasonable repeatability, each measurement was repeated three times.

2.5. Lung histology staining and bronchoalveolar lavage fluid (BALF) collection

The lungs were removed and fixed in 4 % paraformaldehyde. Tissue sections were prepared after paraffin embedding. Lung sections were stained with hematoxylin/eosin (HE, Beyotime, C0105S), Masson staining (Beyotime, C0189S), and Alcian blue-periodic acid Schiff (AB-PAS, Solarbio, G1285). The BALF was performed using 0.5 ml pre-cooled phosphate-buffered saline (PBS, Servicebio, G4207) three times. The supernatant was collected after centrifuging to separate the cellular components. The serum was drawn from the left heart and centrifuged at 4 °C and 4000 rpm for 10 min.

2.6. Enzyme-linked Immunosorbent assay (ELISA)

The TNFα, IL-1β, CXCL1, ferritin and hepcidin levels were quantified using ELISA kits (Elabscience, Wuhan, China) according to the instructions.

2.7. Behavioral tests

The Y maze (arm size: length × width × height, 30 × 6 × 15 cm, respectively) was performed to evaluate spatial memory. The mice were placed at the end of one arm of the Y maze and allowed to explore the area freely for 8 min. An arm entry was recorded when the mouse moved both limbs into an arm, and the total number of arms and consecutive entries into three arms were recorded. Alternation was recorded when a mouse entered three distinct arms during an overlapping triplet set. The percentage of spontaneous alternations was calculated by the number of alternations/(total number of incoming arms).

The novel target recognition (NOR) test was performed in a 50 × 50 × 40 cm silver-gray square. The mice were given 8 min to acclimate to the experimental environment by moving freely the day before testing. During testing, the mice explored two identical objects for 8 min, which were placed at equal distances from each other. Following a 1-h intertrial interval, one object was replaced with a novel item, and each mouse

was allowed to alternate exploring for another 8 min. Mouse exploratory behaviors were defined as licking, sniffing, or climbing within 2 cm of an object. The video tracking software Any-maze (Any-maze Technology SA, Stoelting Co., IL, USA) was used to record the exploration of familiar and novel objects within 8 min. The field was cleaned with 70 % ethanol after each training session.

2.8. Brain histology staining

Animals were perfused with pre-cooled normal saline and 4 % paraformaldehyde. The brains were then obtained and fixed overnight in 4 % paraformaldehyde solution, before sectioning and staining with HE and Nissl stain (Servicebio, G1434).

2.9. Western blot (WB)

Western blot analysis has been described previously [31]. The following antibodies were used: GPX4 (Cat#ab125066), PSD95 (Cat# ab18258), Ferritin (Cat#ab75973) and SYP (Cat#ab32127) were purchased from Abcam. XCT(Cat#DF12509) was purchased from Affinity. Sestrin2(Cat#10795-1-AP) was purchased from Proteintech. FPN1(Cat# TD13561) was purchased from Abmart. HNRNPL (Cat# sc-32317) was purchased from Santa Cruz. β-actin (Cat#EM21002) was purchased from HUABIO. Protein bands were obtained by Tianneng Imaging System (Shanghai, China) using an ECL detection system (Epizyme Biomedical Technology, Shanghai, China). The anti-mouse (Cat# SA00001-1) or anti-rabbit IgG HRP-labeled secondary antibody (Cat# SA00001-2) was purchased from Proteintech. ImageJ software (National Institutes of Health) was used to measure the protein band density, which was were normalized to the density of the β-actin. Values are presented as fold-changes of experimental groups compared to controls.

2.10. Quantitative real-time polymerase chain reaction (qRT-PCR)

The primers used in this study are listed in TableS1. TRIzol reagent (Invitrogen, 15596026) was used to extract total RNA. Hifair III 1st Strand cDNA Synthesis SuperMix (Yeasen Biotech, 11141ES10) was used for cDNA synthesis. SYBR Green Master Mix (Yeasen Biotech, 11201ES03) was used for qRT-PCR. Gene expression was quantified via the $2^{-\Delta\Delta Ct}$ method.

2.11. Preparation of cigarette smoke extract (CSE)

CSE was prepared as our previous study [32,33]. The smoke of one cigarette (tar 10 mg; nicotine 0.8 mg; Marlboro Red Label, Longyan Tobacco Industrial co. LTD, Fujian, China) was bubbled into a flask containing 5 mL of pre-warm PBS (37 °C) using a vacuum pump at a steady flow rate. Each cigarette was smoked for 5 min. Once the cigarette smoke had fully dissolved in the absorption solution, we measured the pH and adjusted it to approximately 7.40 using 1 mol/L NaOH. The solution was then filtered through a 0.22 μm microporous membrane (Merck Millipore, SLGS033SS) to remove bacteria and particulates. For quality control, the solution was standardized by monitoring the absorbance at 320 nm (A320) and 540 nm (A540). CSE quality was accepted if ΔOD (A320-A540) was between 0.9 and 1.2 [34]. The resulting solution was regarded as 100 % CSE. Meanwhile, to avoid batch differences and repeated freezing and thawing, after preparing CSE, we will aliquot it and store it in −80 °C refrigerator. And each time we dilute it, we use an unopened CSE sample. The solution was diluted with medium for use in experiments within 1 h.

2.12. Cell culture

HT22 cells were obtained from Wuhan Pricella Biotechnology Co., Ltd. They were cultured in Dulbecco's modified Eagle medium (Gibco, 11965092) supplemented with 10 % fetal bovine serum (Gibco, 10270-106) and 1 % antibiotic-antimycotic (Invitrogen Corporation, Carlsbad, CA, USA) at 37 °C and 5 % CO_2.

2.13. Cell counting Kit-8 (CCK-8)

HT22 cells were plated in 96-well plates at a density of 5×10^3/well. CCK-8 working solution (Beyotime, C0041) was added to the cells after treatment, and the absorbance at 450 nm was measured by microplate photometer (Bio-Tek Elx800, USA) after 1 h at 37 °C.

2.14. Transmission electron microscopy (TEM)

Fresh hippocampal CA1 tissues and HT22 cells were collected and fixed at 2.5 % glutaraldehyde at 4 °C overnight, followed by postfixed with 1 % osmium tetroxide (OsO4) at 4 °C. After dehydration with alcohol, samples were embedded in epoxy resin, and ultrathin sections were prepared using ultramicrotomy. The sections were stained with uranyl acetate and lead citrate. Ultrastructural images were acquired using a transmission electron microscope (Thermo Scientific, Talos L120C G2).

2.15. Lipid peroxidation assay

Lipid peroxidation was analyzed using C11-BODIPY 581/591 (Invitrogen, D3861) following the manufacturer's instructions.

2.16. Determination of malondialdehyde (MDA) and glutathione (GSH) levels

GSH assay kits (Nanjing Jiancheng, A006-2-1) and MDA assay kits (Beyotime, S0131S) were used following the manufacturer's instructions.

2.17. Measurement of iron

The total iron and Fe^{2+} levels in the hippocampus tissues of mice were measured by an iron assay kit (Dojindo, Kumamoto, Japan, I291) according to the product instructions. The total iron of cells was measured using Cell Total Iron Colorimetric Assay Kit (Elabscience, E-BC-K880-M). The Fe^{2+} of cells was measured using an iron Colorimetric Assay Kit (Applygen, E1046). The total iron of human serum was measured using Total lron Colorimetric Assay Kit (Elabscience, E-BC-K772-M). The Fe^{2+} of human serum was measured using Ferrous lron Colorimetric Assay Kit (Elabscience, E-BC-K773-M).

2.18. Mitochondrial function assessments

To evaluate the mitochondrial membrane potential(MMP), the HT22 cells were stained with JC-1 dye from the JC-1 MitoMP detection kit(Dojindo, Kumamoto, Japan) according to the manufacturer's guidelines. JC-1 in its monomeric cytoplasmic form emits green light, whereas JC-1 in its aggregated form in the mitochondrial membrane emits red light. The transformation of JC-1 from red fluorescence to green fluorescence represents the decrease of mitochondrial membrane potential. Image was captured by a confocal microscope (LSM980, Carl Zeiss, Oberkochen, Germany).The mitoSOX Red probe was used to determine the levels of mitochondrial ROS, according to the manufacturer's protocol (Invitrogen, M36008). The fluorescent intensities were recorded using a multifunction microplate reader (TECAN Infinite M200 Pro, Switzerland). The concentration of ATP was determined using the Enhanced ATP Assay Kit (Beyotime Biotechnology, S0027, China) following the manufacturer's instructions. The luminescence was immediately quantified employing an automatic microplate reader (PerkinElmer, EnSpire, USA).

2.19. RNA-sequencing and bioinformatics analysis

Briefly, total RNA of NC and CSE treated HT22 cell were extracted. RNA-seq was performed using Illumina Novaseq 6000 platform. The retrieved data was compared to the reference genome using HISAT2 aligner, and FPKM of each gene was calculated and the read counts of each gene were obtained by HTSeq-count. The transcriptome sequencing was conducted by OE Biotech Co., Ltd. (Shanghai, China).

Two microarray datasets associated with Alzheimer's disease (GSE5281 and GSE28146) from the hippocampus were obtained from the GEO database (https://www.ncbi.nlm.nih.gov/geo/) [35] and then normalized via the "normalize Between Arrays" function of the R package "limma". GSE5281 contained 10 AD and 13 normal hippocampus tissues and was regarded as a training cohort [36]. GSE28146 contained 22 AD and 8 normal hippocampus tissues and was used as a validation cohort [37]. GPL570 (HG-U133_Plus_2) (Affymetrix Human Genome U133 Plus 2.0 Array) was the platform of these datasets. Differentially expressed genes (DEGs) were identified using the R package 'limma' [38]. Genes exhibiting a $\log_2$ fold-change >1.5 or <-1.5, with an adjusted P-value<0.05, were considered DEGs. Ferroptosis-related genes were obtained from the FerrDb database [39]. The GEPIA database was used to analyze the gene expression correlation in the hippocampus tissue data of GTEx [40].

2.20. Immunofluorescence (IF)

Immunofluorescence assays were conducted on paraffin-embedded tissue sections and HT22 cells. The tissue sections were deparaffinized, rehydrated, and subsequently blocked with 20 % normal goat or donkey serum. A suitable dilution of primary antibodies was used, followed by the fluorescent secondary antibodies Alexa Fluor® 594 goat anti-rabbit IgG H&L (Abcam, ab150080). The nuclei were counterstained with DAPI (Beyotime, P0131). Slides were scanned using Pannoramic MIDI II from 3DHISTECH. HT22 cells were fixed with 4 % paraformaldehyde (Beyotime, P0099) and permeabilized with 0.5 % Triton X-100 (Beyotime, P0096). The cells were blocked with 2 % bovine serum albumin and then incubated with primary antibodies at 4 °C overnight. The secondary antibodies Alexa Fluor® 488 goat anti-rabbit immunoglobulin IgG (Abcam, ab150077) or Alexa Fluor® 594 goat anti-mouse IgG (Abcam, ab150116) were incubated at room temperature for 1 h, and DAPI for 10 min at room temperature. Image was captured by a confocal microscope (LSM980, Carl Zeiss, Oberkochen, Germany).

2.21. Gene-editing experiment

Sestrin2 genes were knocked down using the lentiviral CRISPR/Cas9 sgRNA-mediated expression knockdown protocol (GenePharma, Shanghai, China). The HT22 cells were transfected with sg-sestrin2 or sg-NC lentiviral particle solution using FuGene transfection reagent (Promega, USA). The medium was changed to fresh DMEM after 6 h, and HT22 cells were cultured for another 72 h Sestrin2 knockdown cells were obtained via puromycin screening (HB-PU-500, HanBio Co., Ltd), and the deficient efficiency of sestrin2 was tested by western blotting. The Flag-tagged sestrin2 overexpression and empty plasmids were purchased from GenePharma. Stable overexpressing sestrin2 HT22 cells were generated by transfecting the cells with a sestrin2 overexpression plasmid, followed by selection using puromycin. Stable overexpressing GPX4 and XCT HT22 cells were also generated as described above.

Tsingke Biotechnology (Beijing, China) designed and synthesized HNRNPL and negative control siRNAs. HT22 cells were transfected with HNRNPL or control siRNA using FuGene transfection reagent following the instructions.

2.22. Protein-protein interaction studies

Whole-cell extracts of Flag-sestrin2-transfected 293T cells were collected, and Coimmunoprecipitation (Co-IP) was performed using a Co-IP Kit (Thermo Fisher Scientific, 88804) according to the manufacturer's instructions. In the next step, the Co-IP product was separated by SDS-PAGE. The gel was stained with silver (Solarbio, G7210) and analyzed with liquid chromatography-mass spectrometry (LC-MS). Co-IP was performed using anti-flag antibody (Proteintech,20543-1-AP) or anti-HNRNPL antibody to further confirm the LC-MS analysis results. The HT22 cells were inoculated into a 10-cm cell culture dish. Co-IP was subsequently performed using a Co-IP Kit and then analyzed by western blotting.

2.23. Molecular docking

The GRAMM-X(http://gramm.compbio.ku.edu/) was utilized to dock HNRNPL and sestrin2 proteins to investigate their relationship. The protein structures were obtained from the Uniprot (www.uniprot.org), PDB database (bank PDB: Homepage), and Alphafold database access (https://alphafold.ebi.ac.uk/). Further analysis of protein interactions and visual examination were conducted using Pymol (Version 2.4) and PDBePISA (https://www.ebi.ac.uk/pdbe/pisa/).

2.24. Actinomycin D treatment

Cells were cultured with 2 μg/mL actinomycin D (MedChemExpress, HY-17559) at different times and then the cells were collected after the corresponding times. Afterwards, total RNA was extracted, and the relative expression of GPX4 and XCT was subsequently tested by RT-qPCR.

2.25. Hippocampus adeno-associated virus (AAV) injection

AAV9-sestrin2 and AAV9-NC were designed and purchased from the Shanghai Tsingke. The mice were anesthetized and positioned on the stereotaxic apparatus (RWD Life Science Co. Ltd., Shenzhen, China). AAVs were injected unilaterally in the left hippocampus area above the CA1 region under standard aseptic surgery. The coordinates for injection were as follows: anteroposterior (AP), −2.0 mm; mediolateral (ML), +1.5 mm; dorsoventral (DV), −1.5 mm. When the needle was in place, either AAV9-sestrin2 or AAV9-NC consisting of 0.5 μL viral particles (5.66×10^{13}v.g/mL) was administered at 0.1 μL/min. Following the completion of injection, the needle was left in place for 5 min before removal.

2.26. Statistical analysis

Data were analyzed using GraphPad Prism 9 (San Diego, California) and SPSS 22.0 (IBM, Armonk, NY, USA) software. Statistical significance was determined by $P < 0.05$. Normally distributed data are presented as the mean ± standard deviation (SD) and were compared using a *t*-test. In contrast, non-normally distributed data are reported as median (interquartile range) and analyzed using a nonparametric test. The chi-square test was used to detect differences in qualitative variables, Fisher's exact test, or rank sum test. The correlation analysis was performed using Pearson or Spearman rank correlation analysis.

3. Results

3.1. The hippocampal volume and clinical relevance in patients with COPD

This study initially examined the hippocampus volume and its subregions in 50 patients with COPD and 50 healthy controls. An overview of the baseline characteristics of the subjects is presented in TableS2.

The differences in age, sex, smoking history, and drinking history between the patients with COPD and the controls was not statistically significant. We observed a significant reduction in eTIV (Fig. 1A) and total hippocampal volume (Fig. 1B) among patients with COPD compared to controls. Furthermore, by dividing the hippocampus into 12 subregions using image segmentation techniques, we identified nine subregions that exhibited varying degrees of volume reduction, including CA1, CA3, CA4, GC-ML-DG, HATA, hippocampus fissure, molecular layer, presubiculum and subiculum (Fig. 1C). The representative image is displayed in Fig. 1D. To determine which specific hippocampal subregion is most closely associated with Patients with COPD, as illustrated in Fig. 1E, we found that the degree atrophy of the CA1 and

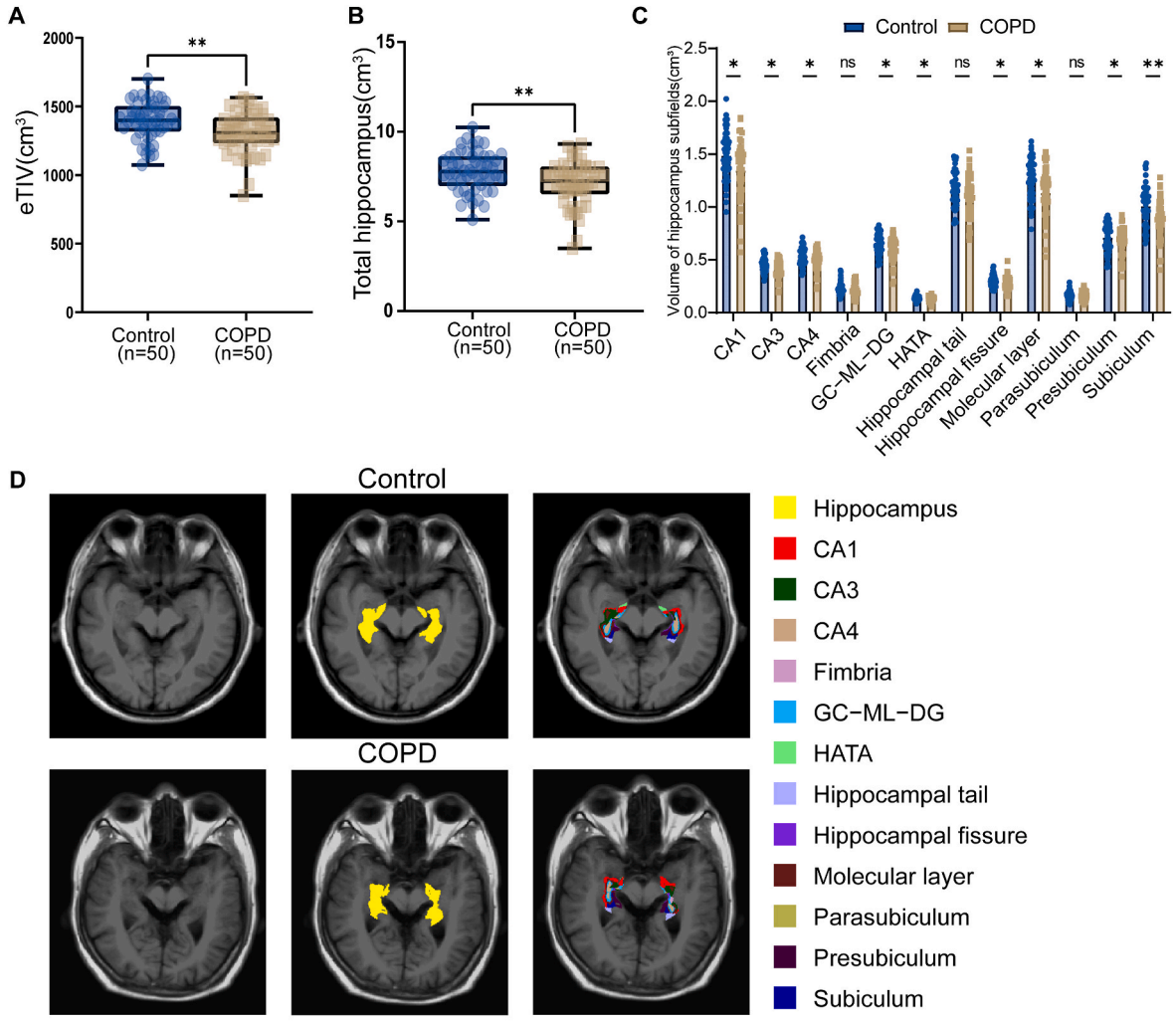

E

Subfields	Control		COPD			
	Mean	SD	Mean	SD	*P*	Log_2FC
CA1	1.49	0.23	1.35	0.27	0.006	-0.144
CA3	0.46	0.07	0.41	0.08	0.007	-0.138
CA4	0.54	0.08	0.49	0.10	0.009	-0.135
Fimbria	0.23	0.06	0.21	0.06	0.245	-0.092
GC-ML-DG	0.64	0.10	0.59	0.11	0.006	-0.136
HATA	0.14	0.02	0.13	0.03	0.029	-0.119
Hippocampal tail	1.17	0.17	1.10	0.19	0.055	-0.090
Hippocampal fissure	0.30	0.05	0.27	0.06	0.020	-0.137
Molecular layer	1.26	0.19	1.13	0.21	0.002	-0.153
Parasubiculum	0.16	0.04	0.16	0.04	0.959	-0.004
Presubiculum	0.71	0.13	0.66	0.13	0.043	-0.113
Subiculum	1.01	0.18	0.88	0.18	<0.001	-0.194

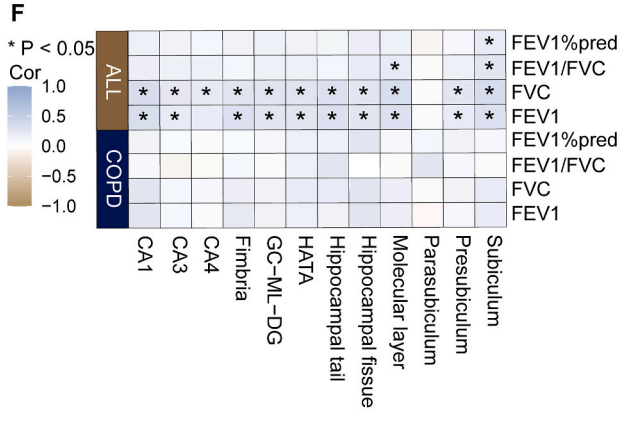

Fig. 1. The volumes and clinical relevance of hippocampus and hippocampal subfields in patients with COPD.
(A)The estimated total intracranial volume comparison. (B) Total hippocampus volume comparison. (C) Comparison of the volume of the hippocampal subregions. (D) Illustration of hippocampal subfield from a representative subject in each group. (E) Listing of the expression profile of hippocampal subfields. (F) Correlation between the volume of the hippocampal subfields and lung function. $^{*}P < 0.05$, $^{**}P < 0.01$.

subiculum was the most obvious, and the CA1 region had the largest volume among the subregions. Subsequently, we explored the correlation between hippocampal subregion volumes and lung function. As depicted in Fig. 1F and TableS3, within all subjects, multiple hippocampal subregions were closely associated with lung function. However, among patients with COPD, only the CA1 region exhibited a potential positive correlation with lung function parameters FEV1 ($r = 0.243$, $P = 0.089$) and FVC ($r = 0.241$, $P = 0.092$). Our results show that the hippocampus volume is reduced in patients with COPD, and that CA1 may be the most closely related brain region.

3.2. Construction of a COPD mouse model

To further explore COPD-related cognitive dysfunction in vivo, we established a murine model of COPD by exposure to CS for 24 weeks. Compared to control mice, CS exposure suppressed weight gain (Fig. 2A), with no significant differences in food intake between the groups (Fig. 2B). The inflammatory factors IL1β, TNFα, and CXCL1 were significantly increased in serum, BALF, and lung tissue (Fig. S1). A marked decline in FEV20/FVC (Fig. 2C) and the FEV20 (Fig. 2D) was also found. Emphysema formation (Fig. 2E), collagen deposition around airways (Fig. 2F), and mucus hyperproduction (Fig. 2G) were also observed in the lung of the COPD mouse model.

3.3. CSE exposure impaired cognitive function and hippocampal neurons

We then evaluated the spatial and working memory of the mice. Compared to controls, CS-exposed mice showed a decreasing trend in the number of arm entries (Fig. 2H) and a decrease in the percentage of spontaneous alternations (Fig. 2I), suggesting that COPD mice exhibit spatial memory impairment. In the NOR test, we observed that both the recognition and discrimination indices were significantly reduced in COPD mice (Fig. 2J and K), indicating impaired working memory. HE staining was then used to observe histopathological changes in the hippocampus. As shown in Fig. 2L, the hippocampal tissue of control mice had a hierarchical structure with clear cell boundaries, regular and complete neuromorphology, and a clear structure of nerve fibers. However, partial loss of hippocampal neurons and partial damage of nerve fibers were observed in CS-exposed mice. The results of Nissl staining showed that CS exposure resulted in a significant loss of neurons in the hippocampal CA1 region in mice (Fig. 2M and N). The mRNA and protein levels of presynaptic protein, synaptophysin (SYP), and PSD95 (postsynaptic protein) were decreased in the hippocampus of CS-exposed mice compared to control mice (Fig. 2O–S).

3.4. LPS + PPE impaired cognitive function and hippocampal neurons

Considering that there are various methods in establishing the model of COPD, we also established an animal model of COPD by LPS combined with PPE, which did not contain nicotine. Compared to control mice, LPS + PPE exposure suppressed weight gain (Fig. S2A). Emphysema (Fig. S2B) were also more pronounced in the lung of the LPS + PPE-exposed mice. A marked decline in the FEV20 (Fig. S2C) and FEV20/FVC (Fig. S2D) was also found. Similar with previous study [41], there was no significant difference in LPS + PPE-exposed mice and the percentage of spontaneous alternations only showed a decreasing trend in LPS + PPE exposed mice (Fig. S2E–F). As for the NOR test, we also observed that both the recognition and discrimination indices were significantly reduced in LPS + PPE-exposed mice (Fig. S2G–H). HE staining showed that partial loss of hippocampal neurons was observed in LPS + PPE-exposed mice (Fig. S2I). Nissl staining showed that LPS + PPE exposure resulted in a decline of neurons in the hippocampal CA1 region (Fig. S2J–K). The protein levels of SYP and PSD95 were also decreased in the hippocampus of LPS + PPE-exposed mice compared to control mice (Fig. S2L–M). These results indicate that although LPS + PPE exposure could cause cognitive dysfunction, the cognitive impairment caused by long-term CS exposure is more significant.

3.5. CSE induced lipid peroxidation and ferroptosis in HT22 cells

To verify the CS-induced damage to hippocampal neurons in vitro, we used CSE to stimulate HT22 cells. The CCK-8 assay demonstrated reduced cell viability with increasing CSE concentrations and times. Among the studied concentrations, 2 % of CSE treated 12h was chosen for their closeness to IC50 on HT22 cells viability (Fig. 3A). Then we performed RNA-sequence analysis on HT22 cells stimulated with CSE for 12 h. The results demonstrated that among various cell death pathways, ferroptosis was more significantly enriched (Fig. 3B).

Then, we explored the cell death patterns at different time. The CCK8 results showed that the ferroptosis inhibitor Ferrostatin-1(Fer-1) alleviated CSE-induced cell death at 12 and 24 h, but its protective effect was more pronounced at 12 h. At 24 h, the protective effect of necroptosis inhibitors Nec-1 became more significant. At 48 h, the degree of cell death was too severe to be mitigated (Fig. 3C). The results of C11-BODIPY indicated that although cell death was more pronounced at 24h, the level of lipid peroxidation was similar to that at 12h. At 48 h, lipid peroxidation further increased (Fig. 3D and E); however, based on the results of CCK8, 48 h was deemed unsuitable. WB showed that at 12h and 24h, ferroptosis markers (GPX4, XCT) and synaptic proteins (PSD95, SYP) exhibited significant damage. The damage of XCT, GPX4, SYP and PSD95 was not significantly worsened with prolonged time (Fig. 3F–J). Overall, these findings suggest that ferroptosis in HT22 cells occurs early after CSE stimulation, with synaptic proteins being damaged in the early stages. Early intervention may help prevent and mitigate cognitive impairment.

Given to diverse concentration of CSE could impact the pattern of cell death, we next assessed the effects of the ferroptosis inhibitor Fer-1, the necroptosis inhibitor necrostatin-1, and the apoptosis inhibitor Z-VAD-FMK at diverse concentration of CSE. The results of CCK8 reveled that apoptosis was predominant at 1.5 %, ferroptosis inhibitors provided more significant protection against CSE-induced cell death at 2 %, necroptosis became the dominant form at 4 %, and at 6 %, extensive necrosis occurred, which was irreversible (Fig. 3K). The results of C11-BODIPY indicated that lipid peroxidation was enhanced by CSE in a dose-dependent manner (Fig. 3L and M). Western blot analysis showed a stable decline in ferroptosis markers (XCT/GPX4) and synaptic proteins (PSD95/SYP) at 2 % CSE (Fig. 3N–R). Additionally, CSE induced higher MDA, total iron, the intracellular labial iron, and lower GSH, GSH/GSSG ratio in a dose-dependent manner (Fig. 3S–W). Based on the substantial impact of the 2 % CSE treatment, this concentration was chosen for subsequent experiments to investigate the role of ferroptosis.

Shrunken mitochondria with reduced mitochondrial cristae were observed in the hippocampal neuronal cells of CSE-treated HT22 cells or CS-exposed mice via TEM (Fig. 3X and Y). The XCT/GPX4 pathway is a typical ferroptosis pathway. A significant reduction in the protein expression levels of XCT and GPX4 was also observed in the hippocampus of mice exposed to CS, according to the Western blot results (Fig. 3Z–AA). Taken together, our results indicated that CSE can induce hippocampal neuronal ferroptosis both in vitro and in vivo.

3.6. Fer-1 reversed the CSE-induced ferroptosis

Fer-1 treatment reversed the decreases in the levels of XCT, GPX4, and synaptic proteins (PSD95 and SYP) compared to the CSE group (Fig. 4A–E). As expected, CSE exposure induced obvious lipid peroxidation, and superfluous lipid peroxidation was significantly inhibited by Fer-1 (Fig. 4F and G). In addition, MDA, total iron, the intracellular labial iron pool, GSH and GSH/GSSG ratio exhibited similar trends (Fig. 4H–L). The results of TEM revealed that Fer-1 attenuated CSE-induced mitochondrial contraction (Fig. 4M). Moreover, Fer-1 improved the decreased levels of MMP as detected by JC-1 (Fig. 4M) and ATP decline in HT22 cells treated with CSE(Fig. 4N), while Fer-1

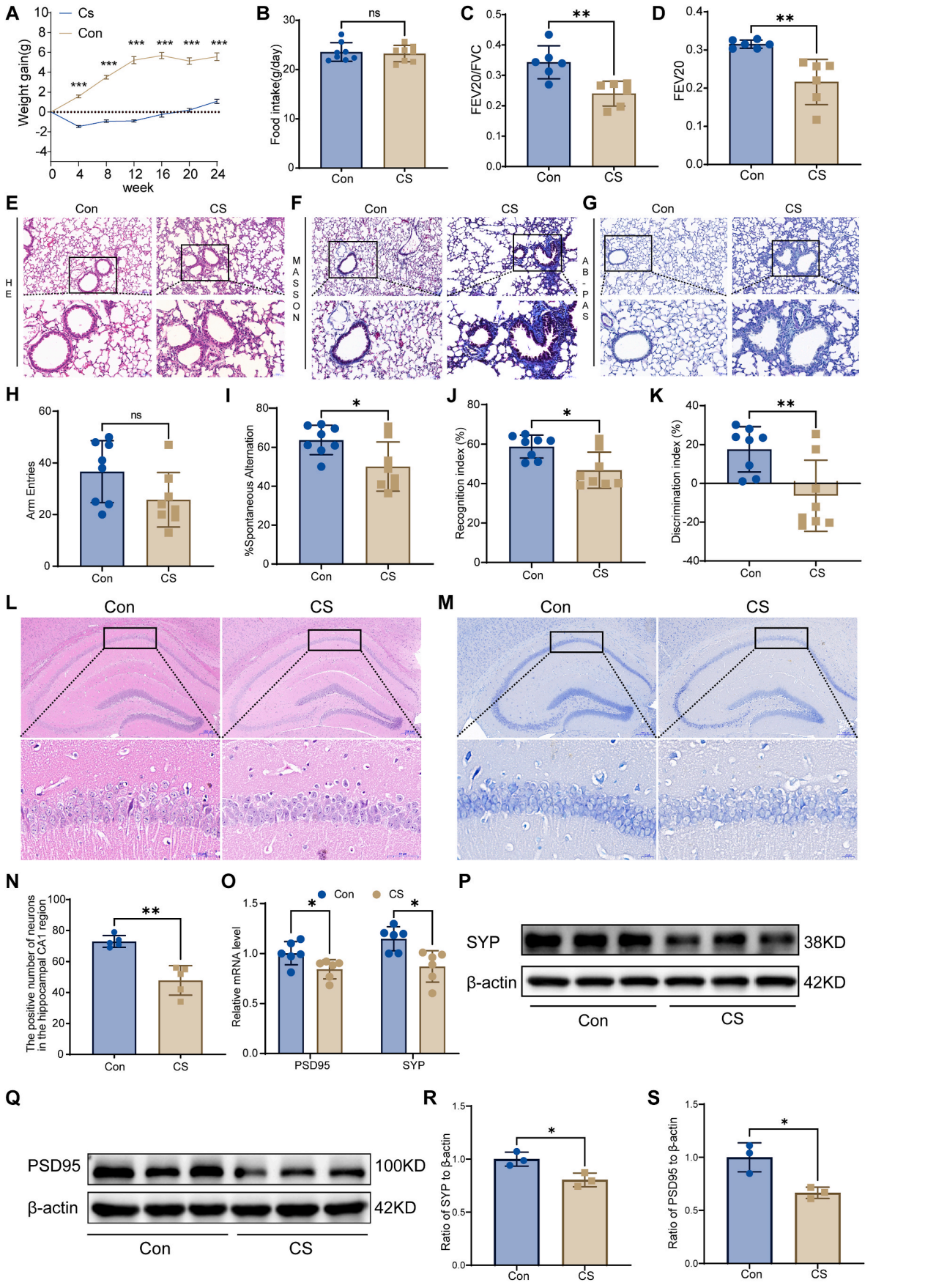

(caption on next page)

Fig. 2. Chronic CS exposure worsened lung function and cognitive function.
(A) Mean body weight gain in each group during the 24 weeks(n = 8). (B) Food intake in each group(n = 8). (C) Comparison of FEV20/FVC in each group(n = 6). (D) Comparison of the FEV20 in each group(n = 6). (E) HE staining of pulmonary tissue of mice (n = 5) (scale bar = 50 μm). (F) MASSON staining of pulmonary tissue of mice (n = 5) (scale bar = 50 μm). (G) AB-PAS staining of pulmonary tissue of mice (n = 5) (scale bar = 50 μm). (H) Arm entries in the Y Maze(n = 8). (I) Percentage spontaneous alternation in Y Maze(n = 8). (J) Recognition index (%) in the NOR test(n = 8). (K) Discrimination index (%) in the NOR test(n = 8). (L) HE staining of hippocampus tissue of mice(n = 5) (scale bar = 50 μm). (M) Nissl staining of hippocampus tissue of mice (n = 5) (scale bar = 20 μm). (N) Quantitative analysis of Nissl body positive cells in the CA1 region. (O) The mRNA expression levels of PSD95 and SYP in the mouse hippocampus of each group. (P) Western blot analysis of SYP levels in mouse hippocampus. (Q) Western blot analysis of PSD95 levels in mouse hippocampus. (R–S) Semiquantitative analysis of SYP and PSD95 in mouse hippocampus of each group. $^{*}P < 0.05$, $^{**}P < 0.01$.

rescued the elevated mitochondrial ROS(mitoROS) due to CSE (Fig. 4O).

We also established HT22 cell lines overexpressing GPX4 (Fig. S3A–B), and the results showed that overexpression of GPX4 restored cell viability (Fig. S3C) and significantly decreased lipid peroxidation level (Fig. S3D–E). The results of TEM revealed that overexpression of GPX4 attenuated CSE-induced mitochondrial contraction (Fig. S3F). Moreover, overexpression of GPX4 also improved the decreased levels of MMP and ATP in HT22 cells treated with CSE (Fig. S3F–G). Overexpressing GPX4 decreases mitoROS and improves mitochondrial function. (Fig. S3H). We also established the HT22 cells overexpressing XCT (Fig. S3I–J). And the overexpression of XCT also restored cell viability and significantly decreased lipid peroxidation level (Fig. S3K–M). These results indicated that CSE inhibited the expression of XCT/GPX4 and eventually led to ferroptosis.

3.7. Sestrin2 is an essential ferroptosis-related gene in cognitive impairment

To identify the essential genes that regulate ferroptosis in cognitive impairment, totally 1046 DEGs were identified after CSE treatment (Fig. 5A). 677 DEGs were identified between the hippocampus in the AD and control groups in GSE5281. Next, In Fig. 5B, the Venn diagram shows only sestrin2 was the ferroptosis-related genes that showed changes in all data. Then, the GSE28146 dataset was used to validate the results. Surprisingly, only sestrin2 was significantly changed (Fig. 5C). Based on GEPIA database analyses, we found that there may be a clear positive correlation between sestrin2 and PSD95, SYP, XCT, and GPX4 (Fig. 5D–G); therefore, we speculate that sestrin2 is involved in CS-induced ferroptosis in the hippocampus. The IF results showed that sestrin2 was significantly induced in expression and localized in the nucleus and cytoplasm (Fig. 5H and I). The Western blot results showed that the expression of sestrin2 increased under CSE stimulation (Fig. 5J and K). As expected, the mRNA (Fig. 5L) and protein expression of sestrin2 in the hippocampus was significantly increased in CS-exposed mice (Fig. 5M and N). The role of sestrin2 in CS-induced ferroptosis requires further investigation.

3.8. Sestrin2 regulates ferroptosis in HT22 cells induced by CSE

We then created stable sestrin2-depleted HT22 cells (sg-sestrin2) to further investigate the effects of sestrin2 on CSE-induced ferroptosis (Fig. 6A and B). As expected, sestrin2 knockdown significantly suppressed XCT/GPX4 expression, aggravating CSE-induced synaptic protein loss (Fig. 6C–G). In addition, sestrin2 knockdown aggravated CSE-induced cell death (Fig. 6H) and CSE-induced lipid peroxidation (Fig. 6I and J). In addition, a further increase in MDA, total iron, Fe^{2+} (Fig. 6K–M) and a decrease in GSH and GSH/GSSG ratio (Fig. 6N and O) were observed in the sg-sestrin2+CSE group. The TEM results showed that sestrin2 knockdown aggravated CSE-induced shrunken mitochondria (Fig. 6P). Sestrin2 knockdown further decreases mitochondrial membrane potential and ATP production (Fig. 6P and Q), and enhances the production of mitoROS in CSE-treated HT22 cell (Fig. 6R).

Subsequently, we established stable sestrin2 overexpressing HT22 cells (OE-sestrin2) (Fig. 7A and B). Western blot showed that the expression of PSD95, SYP, XCT, and GPX4 was increased after sestrin2 overexpression (Fig. 7C–G). The results of CCK8, C11-BODIPY, MDA, total iron and Fe^{2+} showed that OE-sestrin2 cells exposed to CSE restored cell viability and lipid peroxidation, significantly reduced MDA, total iron, Fe^{2+} accumulation and significantly increased GSH and GSH/GSSG ratio compared to HT22 cells exposed to CSE (Fig. 7H–O). The results of TEM revealed that sestrin2 overexpression attenuated CSE-induced mitochondrial contraction (Fig. 7P). In addition, mitochondrial membrane potential and mitochondrial ATP levels were moderately restored by sestrin2 overexpression (Fig. 7P and Q). Overexpression of sestrin2 decreased cellular mitoROS levels during CSE exposure (Fig. 7R). These results indicate that sestrin2 overexpression can significantly inhibit ferroptosis in neuronal cells.

3.9. Sestrin2-HNRNPL complex regulates ferroptosis in HT22 cells induced by CSE

Co-IP experiments were performed to explore the molecular mechanisms by which sestrin2 regulates ferroptosis (Fig. 8A). Mass spectrometry was used to determine the proteins that might bind to sestrin2 (Fig. 8B). Enrichment analysis revealed that proteins highly combined with sestrin2 are primarily enriched in mRNA processing and RNA splicing (Fig. 8C). The results showed that HNRNPL, an RNA-binding protein, binds to sestrin2. Based on GEPIA database analyses, we found that there may be a clear correlation between HNRNPL and sestrin2, PSD95, SYP, XCT, and GPX4 (Fig. 8D–H). Therefore, HNRNPL was selected as a target for further exploration. The molecular docking results revealed that HNRNPL (blue) binds to sestrin2 (yellow) through H-bonds and van der Waals at many sites (Fig. 8I). The binding energy was −16.8 kcal/mol, indicating that HNRNPL and sestrin2 form a stable protein docking model. Western blotting further confirmed that sestrin2 directly binds to HNRNPL (Fig. 8J). Immunofluorescence confocal microscopy confirmed the co-localization of sestrin2 and HNRNPL with or without CSE stimulation (Fig. 8K–M). The results of bioinformatics analysis showed that HNRNPL expression was decreased in the hippocampus of patients with AD and CSE-treated HT22 cell (Fig. 8N and O). Furthermore, we confirmed that the protein expression of HNRNPL was significantly reduced after CS exposure in vivo and in vitro (Fig. 8P–S).

Next, we used siHNRNPL to knock down HNRNPL in normal cells and cell lines stably overexpressing sestrin2 (Fig. 9A and B). The Western blot results showed that the protein levels of PSD95, SYP, XCT, and GPX4 were decreased after HNRNPL knockdown in both ordinary cells and stably overexpressing sestrin2 cell lines (Fig. 9C–G). Compared to CSE-exposed HT22 cells without siHNRNPL, the siHNRNPL group showed a significant increase in lipid peroxidation, total iron and Fe^{2+} accumulation and decreased cell viability, GSH and GSH/GSSG ratio (Fig. 9H–O), with the TEM results showing the same trend (Fig. 9P). Further features are a drop in the mitochondrial membrane potential (Fig. 9P); ATP depletion (Fig. 9Q), and increased mitochondrial ROS after HNRNPL knockdown (Fig. 9R). This suggests that ferroptosis is aggravated after the knockdown of HNRNPL and that the protective effect of sestrin2 is inhibited.

Given to that HNRNPL could regulate mRNA synthesis, transport, and processing, we conducted actinomycin D assays to examine the effects of sestrin2 and HNRNPL on GPX4 and XCT mRNA stability. The results showed that sestrin2 overexpression increased the stability of GPX4 and XCT mRNA, whereas HNRNPL knockdown significantly reduced their stability and abolished the protective effect of sestrin2

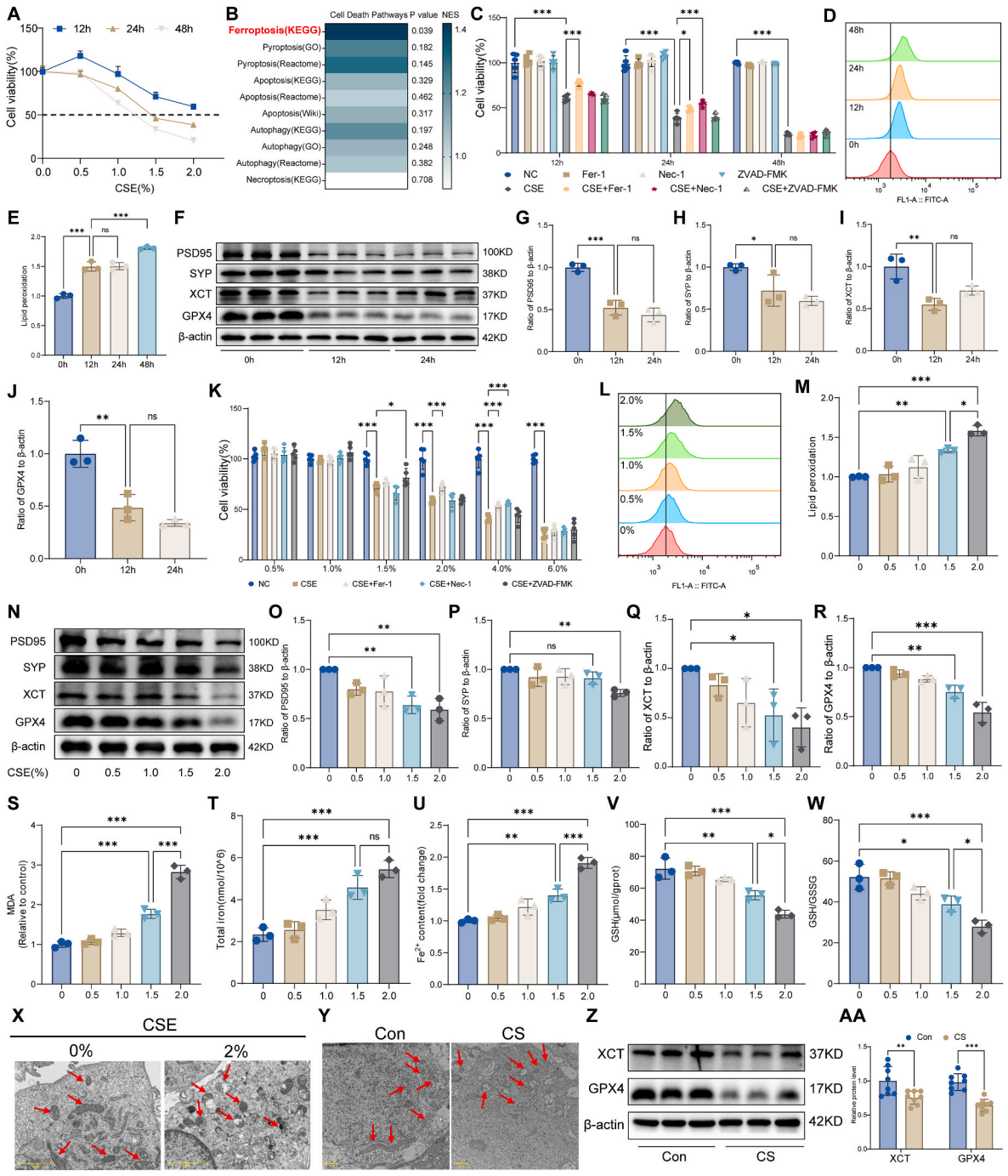

Fig. 3. CSE induced a ferroptotic signature in vivo and in vitro.
(A) CCK-8 assay of HT22 was treated with 0, 0.5 %, 1 %, 1.5 %, and 2 % CSE for 12h,24h and 48h.(B) Heat map of normalized enrichment score (NES) following GSEA of cell death pathway gene lists on RNA-sequence from CSE treated HT22 cells.(C) Cell viability was assessed by CCK-8 assay of HT22 with PBS or 2 % CSE treatment for 12h, 24h and 48h combined with Fer-1 (10 μM), Nec-1(50 μM) or Z-VAD-FMK (20 μM). (D–E) Lipid peroxidation in different times was assayed by flow cytometry using the C11-BODIPY probe. (F–J) Western blot and semiquantitative analysis of PSD95, SYP, XCT, and GPX4 levels of HT22 with 2 % CSE treatment for different times. (K) Cell viability was assessed by CCK-8 assay of HT22 with 0 %,0.5 %,1.0 %,1.5 %,2.0 %,4 %,6 % CSE treatment for 12h combined with Fer-1 (10 μM), Nec-1(50 μM) or Z-VAD-FMK (20 μM). (L–M) Lipid peroxidation in different dose of CSE was assayed by flow cytometry using the C11-BODIPY probe. (N–R) Western blot and semiquantitative analysis of PSD95, SYP, XCT, and GPX4 levels of HT22 with different dose of CSE. (S) MDA levels of HT22 cells. (T) Total iron concentration of HT22 cells. (U) Labial iron pool concentration of HT22 cells. (V) GSH levels of HT22 cells. (W) GSH/GSSG ratio of HT22 cells. (X) Representative TEM images of cells after CSE treatment. (Y) Representative TEM images of mouse hippocampus in each group. (Z-AA) Western blot and semiquantitative analysis of XCT and GPX4 levels in mouse hippocampus. $^{*}P < 0.05$, $^{**}P < 0.01$, $^{***}P < 0.001$.

(Fig. 9S and T). These findings indicate that the sestrin2/HNRNPL protects cells from ferroptosis by maintaining GPX4 and XCT mRNA stability and expression. In summary, sestrin2 can directly bind to HNRNPL and negatively regulate the occurrence of ferroptosis, thereby improving the loss of synaptic proteins.

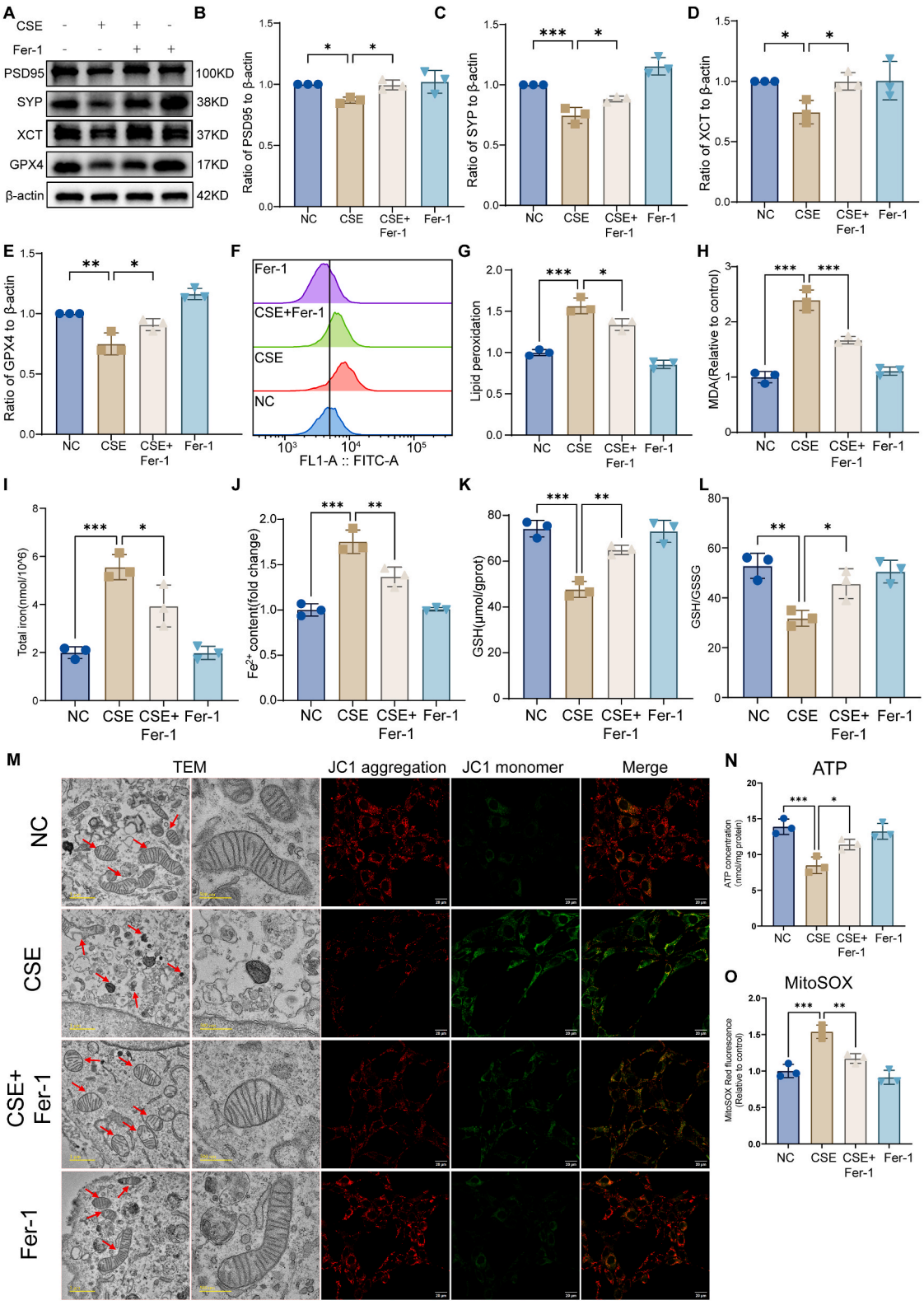

Fig. 4. Fer-1 alleviated CSE-induced ferroptosis.
(A–E) Western blot and semiquantitative analysis of PSD95, SYP, XCT, and GPX4 levels of HT22 with PBS or 2 % CSE treatment for 12h combined with Fer-1 (10 μM). (F–G) Lipid peroxidation was assayed by flow cytometry using the C11-BODIPY probe. (H) MDA levels of HT22 cells. (I) Total iron concentration of HT22 cells. (J) Labial iron pool concentration of HT22 cells. (K) GSH levels of HT22 cells. (L) GSH/GSSG ratio of HT22 cells. (M) Representative TEM images and fluorescence images of JC-1 of cells after CSE and Fer-1 treatment. Red arrows indicate mitochondria. The transformation of JC-1 from red to green represents the decrease of mitochondrial membrane potential. (N) The levels of ATP in each group. (O) The levels of mitoROS detected by mitoSOX red in each group. $^{*}P < 0.05$, $^{**}P < 0.01$, $^{***}P < 0.001$.

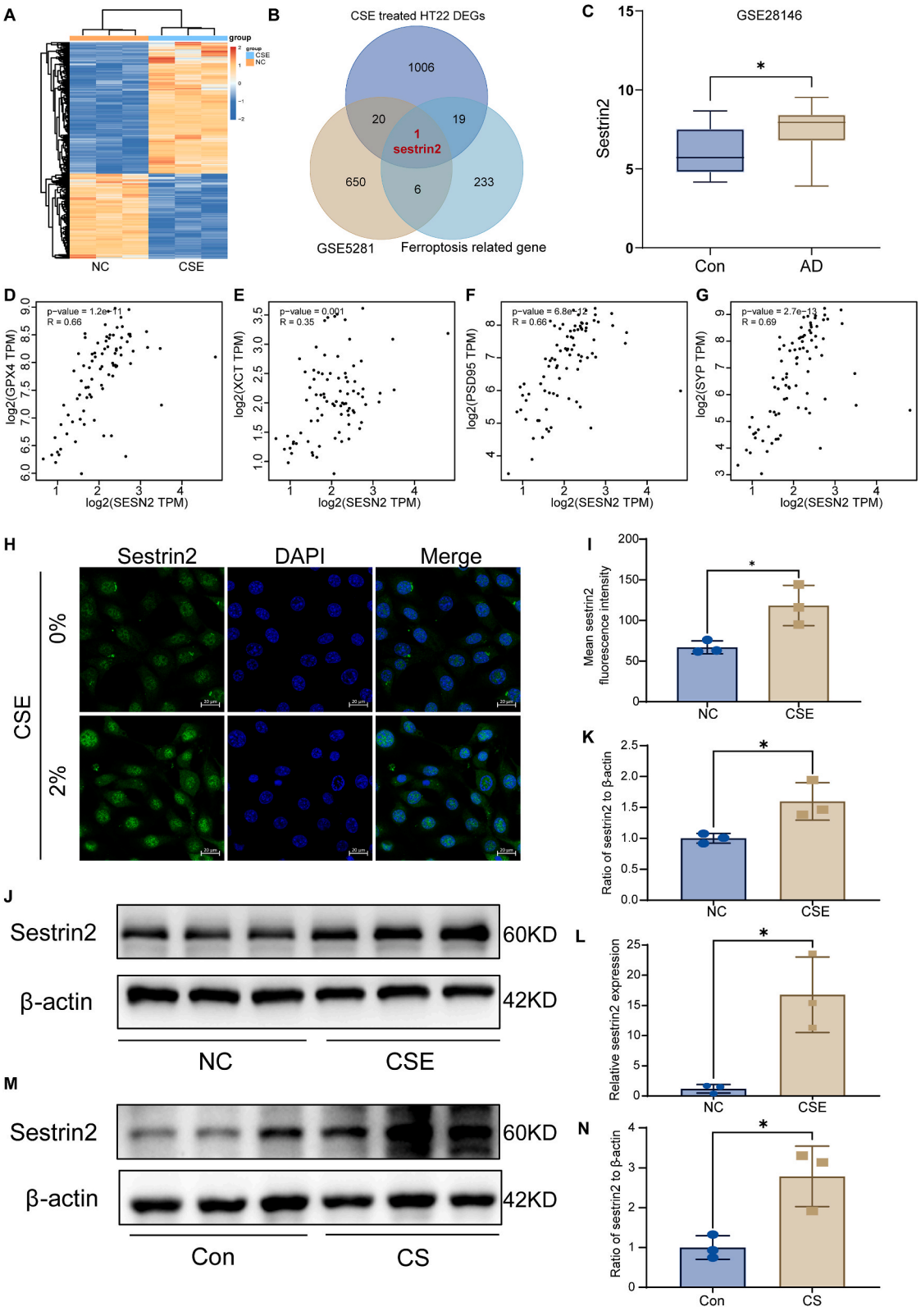

Fig. 5. Sestrin2 is a key upregulated ferroptosis-related gene in the CS exposure model.
(A) The DEGs between HT22 cells with and without CSE treated are shown in the heatmap. (B)Venn diagram showing the intersection of ferroptosis-related genes, DEGs in GSE5281 and DEGs in CSE-treated HT22. (C)The expression of sestrin2 in GSE28146. (D) Protein-protein interaction between sestrin2 and GPX4 based on the GEPIA database. (E) Protein-protein interaction between sestrin2 and XCT based on the GEPIA database. (F) Protein-protein interaction between sestrin2 and PSD95 based on the GEPIA database. (G) Protein-protein interaction between sestrin2 and SYP based on the GEPIA database. (H) Sestrin2 Immunofluorescence staining in HT22 cells after CSE treatment (scale bar = 20 μm). (I) Results of average fluorescence intensity of the sestrin2. (J–K) Quantification and representative immunoblot analysis of sestrin2 in CSE-treated HT22 cells. (L) The mRNA expression levels of sestrin2 in CSE-treated HT22 cells. (M – N) Quantification and representative immunoblot analysis of sestrin2 in mouse hippocampus of each group. *$P < 0.05$.

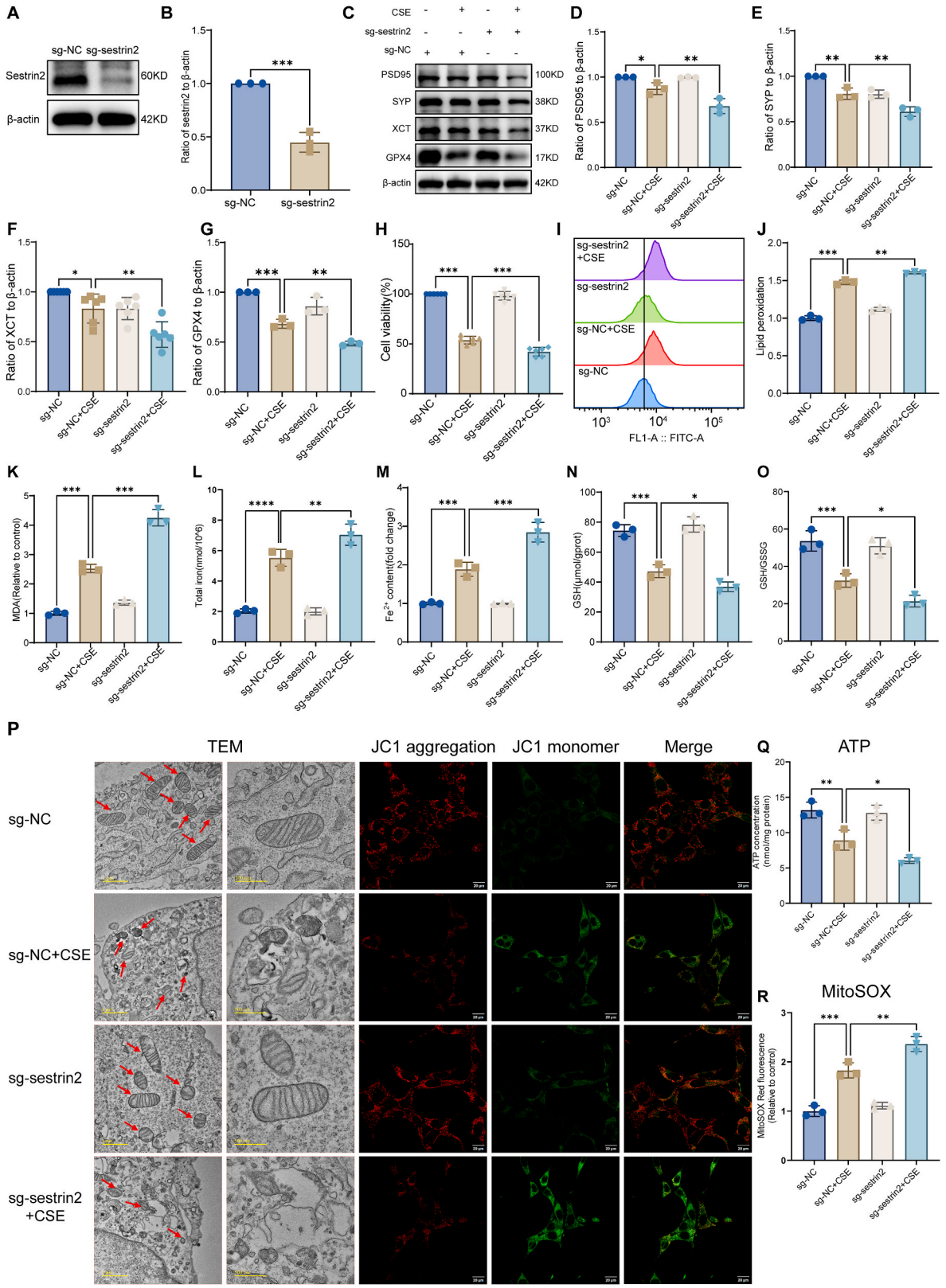

Fig. 6. Effects of sestrin2 knockdown on ferroptosis in CSE-treated HT22 cells.
(A–B) Western blot verification of sestrin2 knockdown in HT22 cells. (C–G) Western blot and semiquantitative analysis of PSD95, SYP, XCT, and GPX4 in cells after treatment with CSE. (H) Cell viability was assessed by CCK-8 assay in cells after treatment with CSE. (I–J) Lipid peroxidation was assayed by flow cytometry using the C11-BODIPY probe. (K) MDA levels of HT22 cells. (L) Total iron concentration of HT22 cells. (M) Labial iron pool concentration of HT22 cells. (N) GSH levels of HT22 cells. (O) GSH/GSSG ratio of HT22 cells. (P) Representative TEM images and fluorescence images of JC-1 of HT22 cells. Red arrows indicate mitochondria. The transformation of JC-1 from red to green represents the decrease of mitochondrial membrane potential. (Q)The levels of ATP in each group. (R) The levels of mitoROS detected by mitoSOX red in each group. $^{*}P < 0.05$, $^{**}P < 0.01$, $^{***}P < 0.001$.

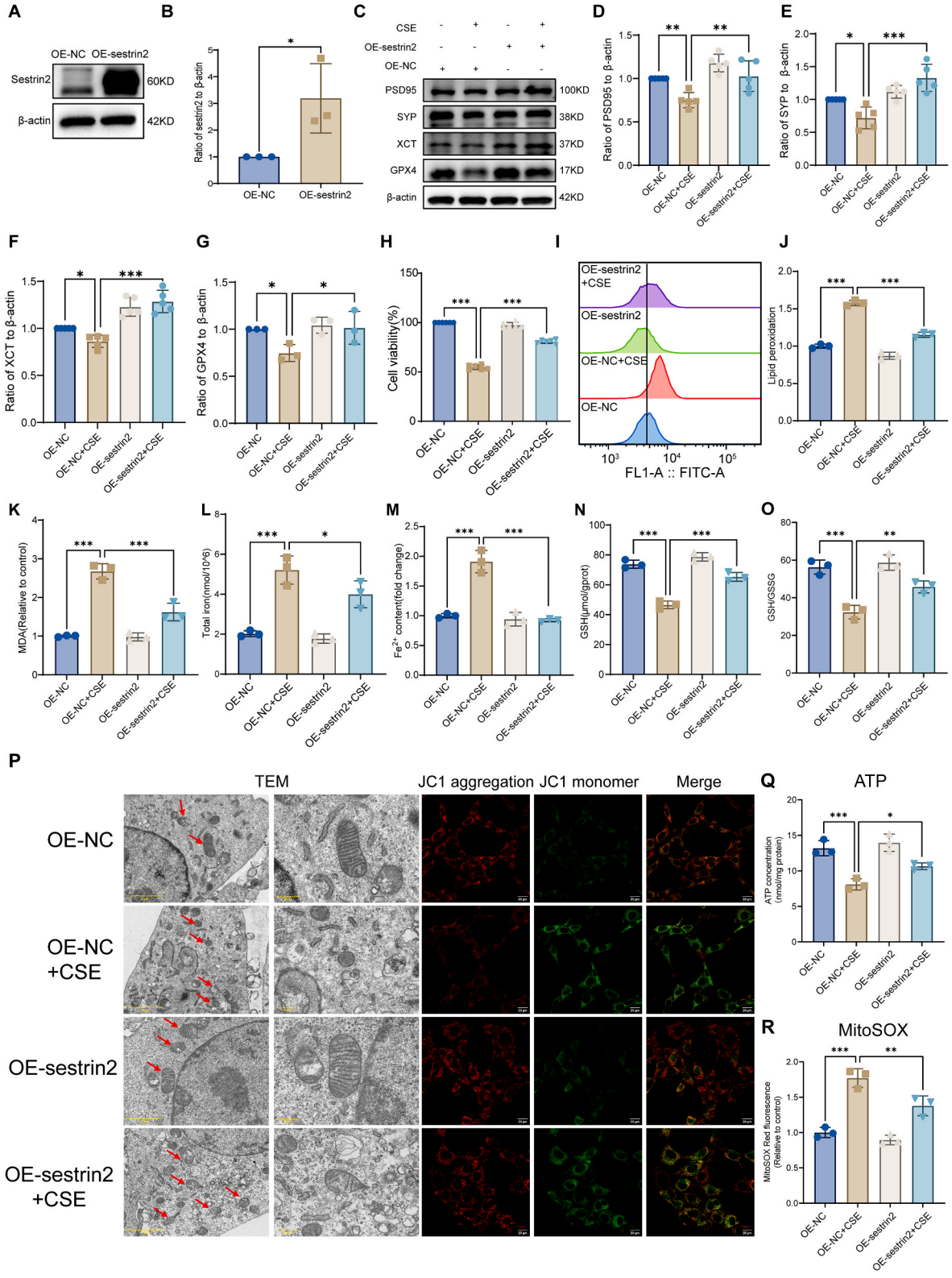

Fig. 7. Effects of sestrin2 overexpression on ferroptosis in CSE-treated HT22 cells.
(A–B) Western blot verification of sestrin2 overexpression in HT22 cells. (C–G) Western blot and semiquantitative analysis of PSD95, SYP, XCT, and GPX4 in cells after treatment with CSE. (H) Cell viability was assessed by CCK-8 assay in cells after treatment with CSE. (I–J) Lipid peroxidation was assayed by flow cytometry using the C11-BODIPY probe. (K) MDA levels of HT22 cells. (L) Total iron concentration of HT22 cells. (M) Labial iron pool concentration of HT22 cells. (N) GSH levels of HT22 cells. (O) GSH/GSSG ratio of HT22 cells. (P) Representative TEM images and fluorescence images of JC-1 of HT22 cells. Red arrows indicate mitochondria. The transformation of JC-1 from red to green represents the decrease of mitochondrial membrane potential. (Q)The levels of ATP in each group. (R) The levels of mitoROS detected by mitoSOX Red in each group. $^{*}P < 0.05$, $^{**}P < 0.01$, $^{***}P < 0.001$.

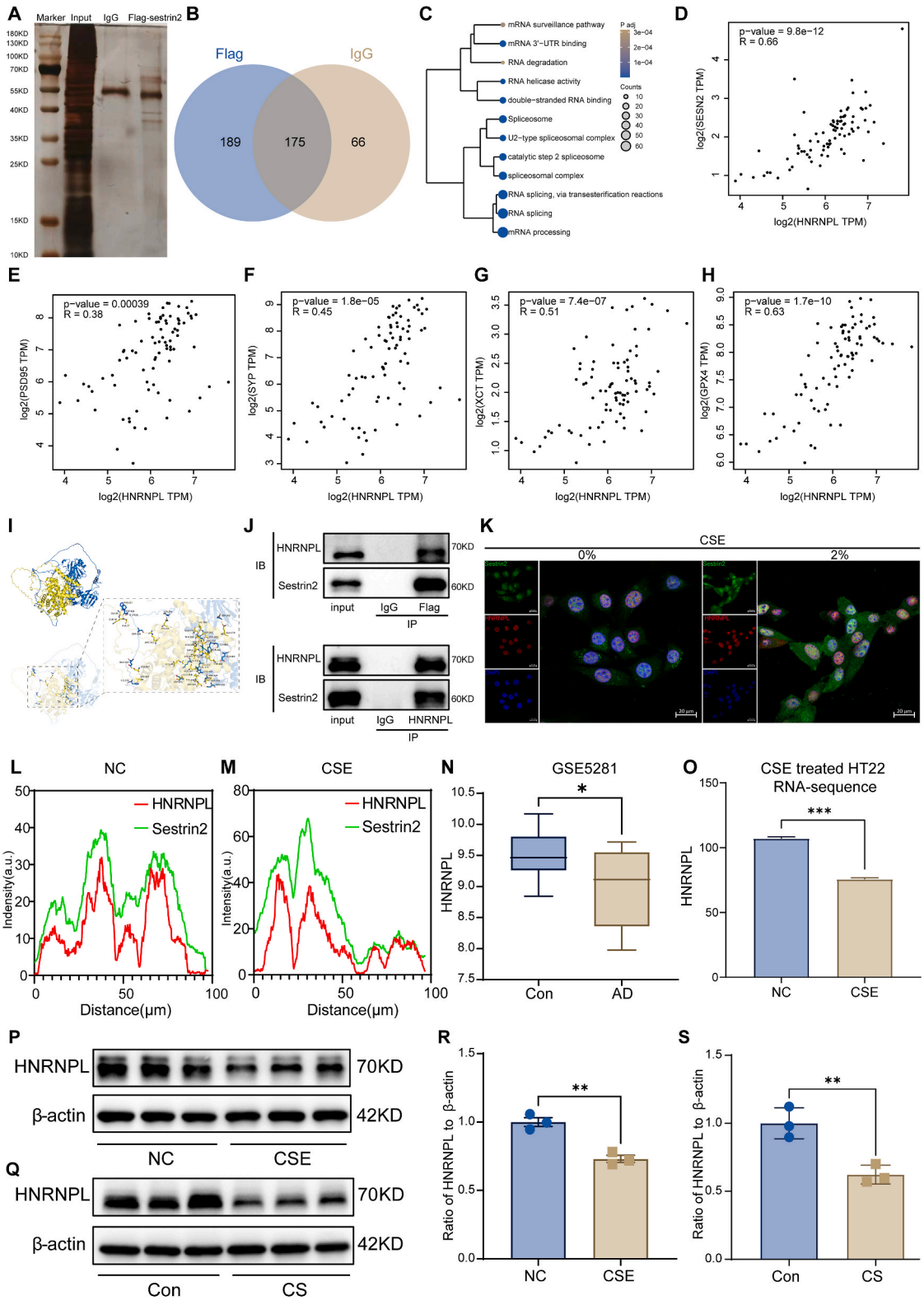

Fig. 8. Sestrin2 is combined with HNRNPL.

(A) Silver stained SDS-PAGE of Co-IP samples. Cellular extracts from 293T cells stably expressing FLAG-sestrin2 were subjected to affinity purification with anti-FLAG affinity columns and eluted with FLAG peptides. (B) Venn diagram of sestrin2 interacting proteins identified by COIP and mass spectrometric analysis. (C) Enrichment analysis was conducted using interacting proteins of LC-MS results. (D–H) Protein-protein interaction between HNRNPL and sestrin2, PSD95, SYP, XCT, and GPX4 based on the GEPIA database. (I) Molecular docking model of sestrin2 (yellow) interacting with HNRNPL (blue). (J) Co-IP assays were performed in sestrin2 overexpression HT22 cells with anti-Flag or anti-HNRNPL, followed by immunoblotting (IB). (K) The Immunofluorescence co-localization assay of sestrin2 (green) and HNRNPL (red) (scale bar = 20 μm). (L–M) Plots of pixel intensity of Immunofluorescence images. (N) The expression of HNRNPL in GSE5281. (O) The expression of HNRNPL in RNA-sequence of CSE-treated HT22 cells. (P, R) Western blot and semiquantitative analysis of HNRNPL levels in CSE-treated HT22 cells. (Q, S) Western blot and semiquantitative analysis of HNRNPL levels in mouse hippocampus. $^{*}P < 0.05$, $^{**}P < 0.01$, $^{***}P < 0.001$.

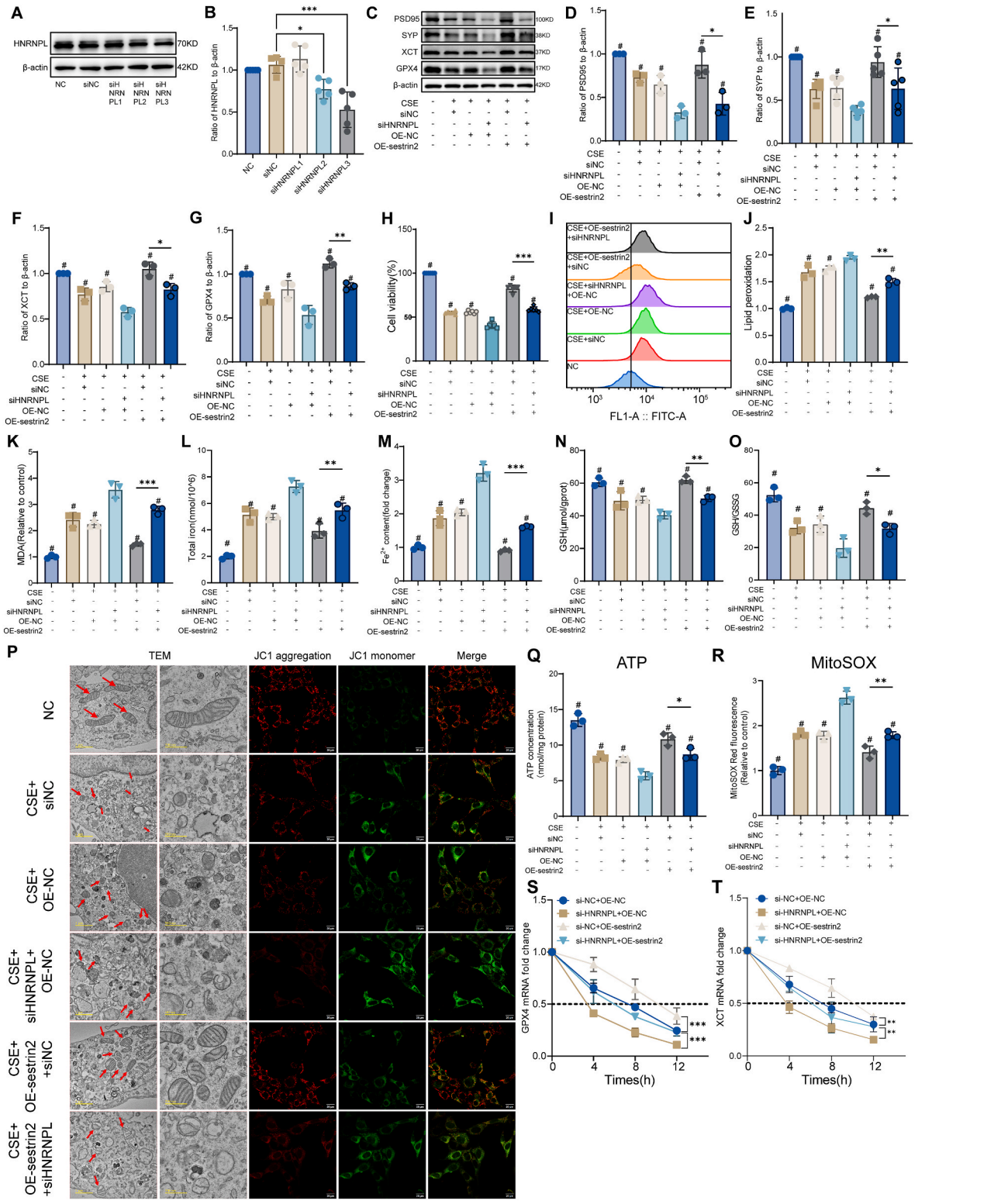

Fig. 9. Sestrin2 regulates ferroptosis by binding with HNRNPL.
(A–B) Western blot verification of HNRNPL knockdown in HT22 cells. (C–G) Western blot and semiquantitative analysis of PSD95, SYP, XCT, and GPX4 in cells after treatment with CSE. (H) Cell viability was assessed by CCK-8 assay in cells after treatment with CSE. (I–J) Lipid peroxidation was assayed by flow cytometry using the C11-BODIPY probe. (K) MDA levels of HT22 cells. (L) Total iron concentration of HT22 cells. (M) Labial iron pool concentration of HT22 cells. (N) GSH levels of HT22 cells. (O) GSH/GSSG ratio of HT22 cells. (P) Representative TEM images and fluorescence images of JC-1 of HT22 cells. Red arrows indicate mitochondria. The transformation of JC-1 from red to green represents the decrease of mitochondrial membrane potential. (Q)The levels of ATP in each group. (R) The levels of mitoROS detected by mitoSOX Red in each group. (S–T) RT-qPCR detection of GPX4 and XCT mRNA in four groups (Vector, siHNRNPL, OE-sestrin2 and siHNRNPL + OE-sestrin2) with or without actinomycin D treatment. $^{*}P < 0.05$, $^{**}P < 0.01$, $^{***}P < 0.001$; $^{\#}P < 0.05$ versus CSE + siHNRNPL group.

3.10. CSE causes iron metabolism imbalance

To further clarify the effect of CS exposure on iron metabolism, we examined the changes of Ferritin, FPN1, hepcidin (HAMP) and IL6(Key inflammatory factor that induce HAMP expression). The results showed that the levels of ferritin, HAMP and IL6 was increased, and the level of FPN1 was decreased in both CS-exposed mice (Fig. 10A–C). The same trend was observed in CSE-stimulated HT22 cells, and the above changes were reversed when ferroptosis inhibitors DFO and Fer-1 were added (Fig. 10D–F). Meanwhile, after overexpression of sestrin2, Ferritin, HAMP and IL6 levels decreased, and FPN1 protein levels increased, while the protective effect of sestrin2 was blocked after HNRNPL was knocked down (Fig. 10G–I). Similarly, at the clinical level, we found compared to control, a decrease in serum iron and ferrous, and an increase in ferritin, hepcidin, and IL6 expression was found in patients with COPD(Fig. 10J–N).

3.11. DFO attenuates cognitive impairment in COPD mice

After identifying the abnormality of iron metabolism, we investigated the effect of iron chelater DFO on cognitive function in COPD mice. DFO had marginal impact on body weights of treated mice

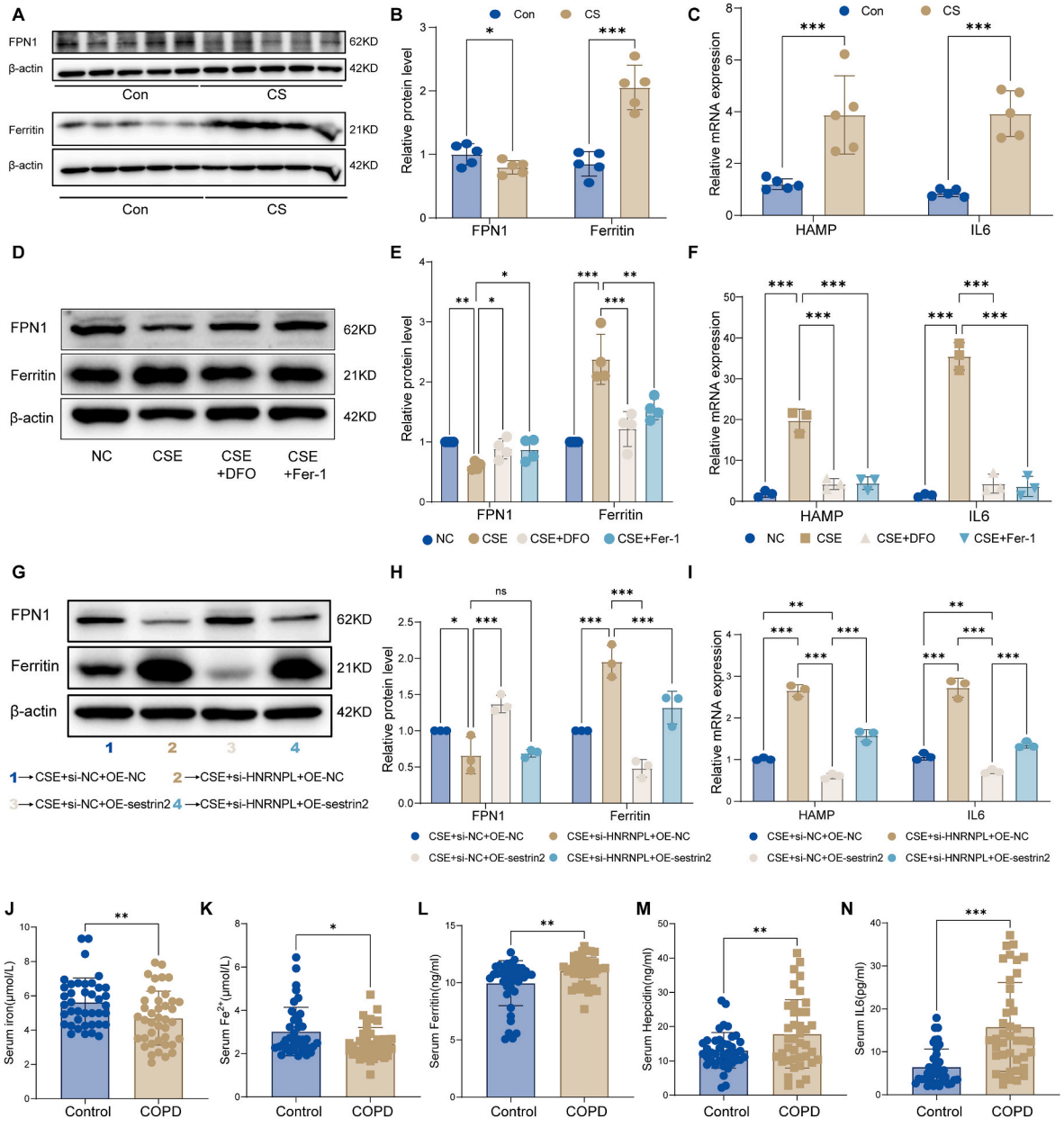

Fig. 10. Effect of CS exposure on iron metabolism.
(A–B) Western blot and semiquantitative analysis of FPN1 and ferritin in mouse hippocampus. (C) RT-qPCR detection of HAMP and IL6 mRNA in in mouse hippocampus. (D–E) Western blot and semiquantitative analysis of FPN1 and Ferritin in HT22 cells treated with or without 2 %CSE, Fer-1(10 μm) and DFO (100 μm). (F) RT-qPCR detection of HAMP and IL6 mRNA in HT22 cells treated with or without Fer-1(10 μm) and DFO(100 μm). (G–H) Western blot and semiquantitative analysis of FPN1 and Ferritin in four groups (CSE + si-NC + OE-NC, CSE + si-HNRNPL + OE-NC, CSE + si-NC + OE-sestrin2, CSE + si-HNRNPL + OE-sestrin2). (I) RT-qPCR detection of HAMP and IL6 mRNA in four groups (CSE + si-NC + OE-NC, CSE + si-HNRNPL + OE-NC, CSE + si-NC + OE-sestrin2, CSE + si-HNRNPL + OE-sestrin2). (J)The levels of serum iron in control and COPD subjects. (K)The levels of serum Fe^{2+} in control ang COPD subjects. (L)The levels of serum ferritin in control and COPD subjects. (M)The levels of serum hepcidin in control and COPD subjects. (N)The levels of serum IL6 in control and COPD subjects. *$P < 0.05$, **$P < 0.01$, ***$P < 0.001$.

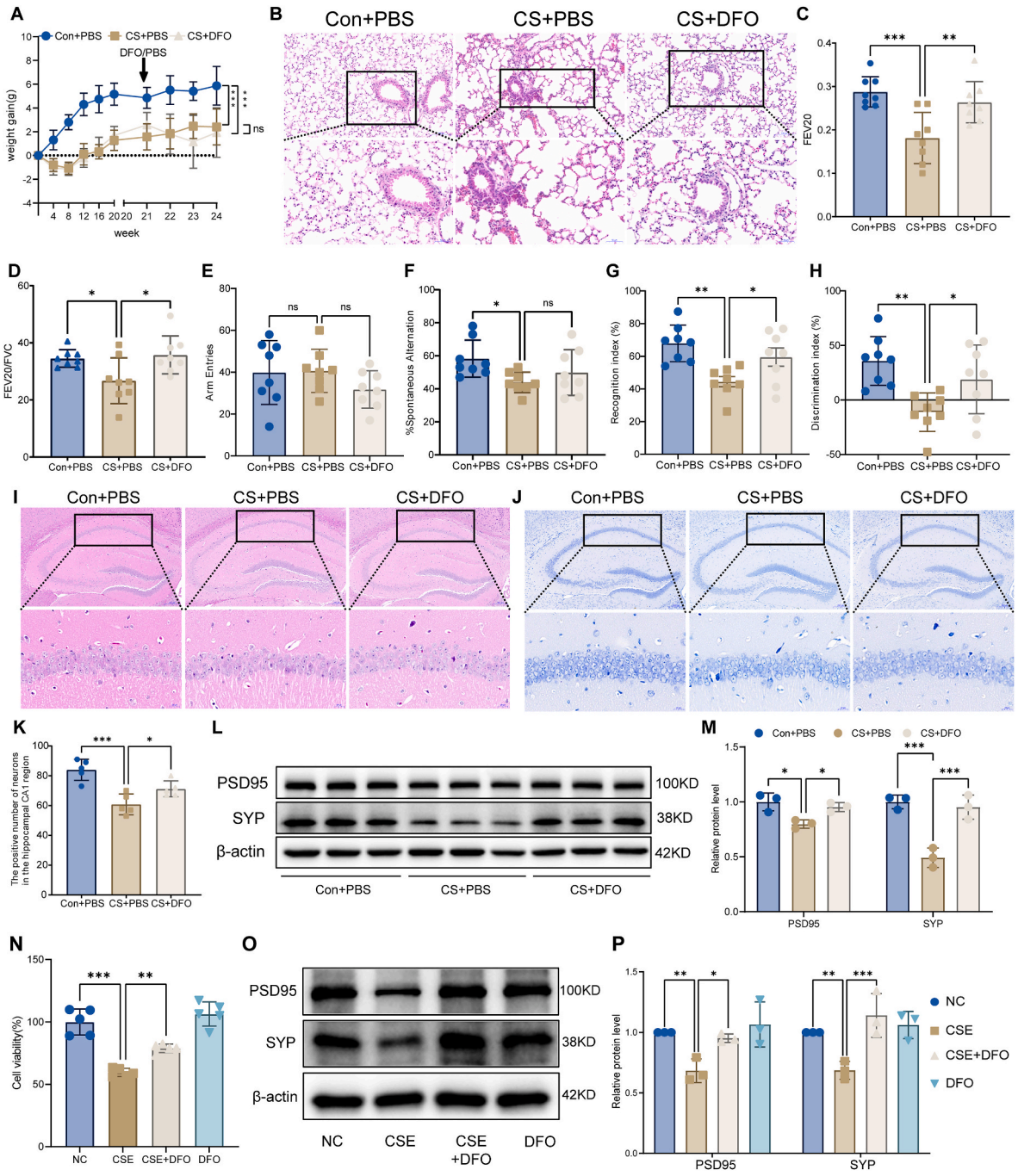

Fig. 11. DFO attenuates CS-induced cognitive deficits.
(A) Mean body weight gain in each group during the 24 weeks(n = 8). (E) HE staining of pulmonary tissue of mice (n = 5) (scale bar = 50 μm). (C) Comparison of the FEV20 in each group(n = 8). (D) Comparison of FEV20/FVC in each group(n = 8). (E) Arm entries in the Y Maze(n = 8). (F) Percentage spontaneous alternation in Y Maze(n = 8). (G) Recognition index (%) in the NOR test(n = 8). (H) Discrimination index (%) in the NOR test(n = 8). (I) HE staining of hippocampus tissue of mice (n = 5) (scale bar = 20 μm). (J) Nissl staining of pulmonary tissue of mice (n = 5) (scale bar = 20 μm). (K) Quantitative analysis of Nissl body positive cells in the CA1 region. (L–M) Western blot and semiquantitative analysis of PSD95 and SYP in the hippocampus of each group. (N) Cell viability was assessed by CCK-8 assay in HT22 cells treated with or without 2 %CSE and DFO (100 μm). (O–P) Western blot and semiquantitative analysis of PSD95 and SYP in HT22 cells treated with or without 2 %CSE and DFO (100 μm). $^{*}P < 0.05$, $^{**}P < 0.01$, $^{***}P < 0.001$.

(Fig. 11A). HE staining of lung tissue showed that DFO significantly alleviated emphysema and airway inflammation (Fig. 11B). Lung function indicators FEV20 and FEV20/FVC were also improved (Fig. 11C and D). Y Maze results showed that DFO did not improve spatial memory significantly (Fig. 11E and F). The results of the NOR test showed that DFO significantly improved the working memory of mice with COPD (Fig. 11G and H). HE and Nissl staining results showed that DFO alleviated the neurological impairment of COPD (Fig. 11I–K). PSD95 and SYP expression was significantly higher in the CS + DFO groups than in the CS + PBS group (Fig. 11L and M). In vitro, DFO equally rescued cell death induced by CSE (Fig. 11N). The expression levels of PSD95 and SYP by Western blot analysis were significantly reduced in HT22 cells treated with CSE, but rescued by DFO (Fig. 11O and P).

3.12. AAV9-mediated sestrin2 overexpression attenuates CS-induced cognitive dysfunction in mice

To examine the neuroprotective effects of sestrin2 overexpression in COPD mice, we administered AAV-sestrin2 or AAV-NC via hippocampal injection at week 20, as illustrated in Fig. 12A. No significant difference was observed in body weight between CS + AAV-sestrin2 and CS + AAV-NC (Fig. 12B). Similarly, AAV injection had no overall effect on weight, suggesting administration of AAV to mice had no obvious toxic effect and mice gained weight normally. Four weeks after injection, we confirmed the transfection efficiency of AAV-sestrin2 in the CA1 region of the hippocampus using Western blot analysis (Fig. 12C and D) and immunofluorescence staining (Fig. 12E). Notably, the Y-maze tests revealed no statistically significant differences in the number of arm entries among the three groups (Fig. 12F), and sestrin2 overexpression partially alleviated the decrease in the percentage of spontaneous alternations in COPD mice (Fig. 12G). The NOR test results showed that sestrin2 overexpression significantly improved the CS-induced decline in recognition and discrimination indexes (Fig. 12H and I). Regarding hippocampal pathology, HE and Nissl staining results showed that compared to the CS group, sestrin2 overexpression prevented CS-induced neuropathological changes in the mouse hippocampus (Fig. 12J–L). We then demonstrated that sestrin2 overexpression suppressed cigarette-induced hippocampus ferroptosis, as indicated by decreased concentrations of MDA, total iron and Fe^{2+} and elevated GSH and GSH/GSSG ratio levels (Fig. 12M – P). The TEM images showed that mitochondrial atrophy and cristae loss or reduction were more pronounced in the CS group, while sestrin2 overexpression mice reversed this change (Fig. 12Q). The Western blot results further confirmed that sestrin2 overexpression reversed the cigarette-induced decrease in XCT/GPX4/PSD95/SYP/FPN1 levels and decreased ferritin protein levels (Fig. 12R and S). As expected, a significant reduction of HAMP and IL6 mRNA expression were detected in CS + AAV-sestrin2 compared with CS + AAV-NC mice (Fig. 12T). These findings indicate that the overexpression of sestrin2 mediated by AAV9 in the hippocampus reverses ferroptosis and synaptic damage induced by CS.

4. Discussion

COPD is a heterogeneous and multicomponent disease that affects more than solely the lungs. To date, cognitive dysfunction has been of increasing interest due to its impact on prognosis and life quality. However, studies focusing on exploring the specific molecular mechanisms of COPD-related cognitive dysfunction remain limited. It has recently been suggested that, except for persistent systemic inflammation, local neurotoxic processes in the brain are important triggers for developing cognitive impairment [15]. Ferroptosis has been implicated in COPD and the occurrence of its extrapulmonary comorbidities [24,34]. Sestrin2 is an important protein against oxidative stress and provides protection against various stresses, including ferroptosis [26]. In this study, we found that CS-induced ferroptosis primarily results in hippocampus atrophy and spatial and working memory deficits in COPD. Sestrin2 regulates ferroptosis by interacting with HNRNPL to form a functional complex and ultimately mitigates cognitive impairment in a CS-induced mouse model of COPD. Thus, we uncovered a new molecular mechanism of COPD-related cognitive dysfunction, which may contribute to developing and optimizing treatment strategies for COPD-related comorbidities.

Cognitive dysfunction is a common extra-pulmonary complication that seriously affect the quality of life and prognosis of Patients with COPD [7,42]. Structural changes in the hippocampus can exist in the early stage of patients with COPD [9,43,44]. Consistent with previous findings [9,45], we found significant hippocampal atrophy in patients with COPD. The hippocampus is a complex region comprising distinct subregions. Advances in magnetic resonance technology and computer algorithms have made it possible to segment hippocampal subregions. We demonstrated for the first time that there were varying degrees of shrinkage in the volume of hippocampal subregions in patients with COPD, with the most significant changes observed in the CA1 and subiculum regions. Takahashi [29] found that in patients with COPD, the volume of the CA1 region was correlated with the WHO/QOL-26 score, which reflects life quality, and the volume of the subiculum was related to the KCL score, which reflects the degree of frailty. These findings further suggest the importance of CA1 and the subiculum in the development of brain-related comorbidities in patients with COPD. The hippocampal CA1 area is the most prone to lesions and plays a vital role in the generation of learning and memory [46]. The subiculum is the main output structure, receiving information input from the olfactory cortex in the CA1 region of the hippocampus and then projecting to multiple downstream brain regions [47]. Therefore, the CA1 region may be the core area of hippocampal injury in patients with COPD. At the same time, correlation analysis showed that in the whole subject, the hippocampal subregion had a certain correlation with the changes in lung function, whereas in the COPD group, we found a potential correlation between the CA1 region and the changes of lung function, similar to our previous results [9]. More clinical samples are needed to confirm this result. In addition to the hippocampus, patients with COPD also showed significant structural changes in cortical regions. Chen et al. pioneered the decomposition of the structure of the cerebral cortex into cortical thickness, surface area (SA) and cortical wrinkles to establish a complete profile of brain injury in COPD patients; and found the SA decreased in the motor, parietal and prefrontal cortex, especially in the dorsomedial prefrontal cortex and Broca's area [48]. Our previous studies also found that the default mode network(DMN) of the overall brain was weakened in COPD patients, especially in the hippocampus, posterior cingulate gyrus, and superior limbic gyrus, which are closely related to memory integration [49], as well as reduced gray matter density and extensive white matter damage [50]. These findings showed that early changes in pulmonary function may lead to changes in hippocampal volume and cognitive function. Patients with early-stage COPD are frequently ignored owing to the absence of significant symptoms. However, by this time, cognitive function may already be impaired, underscoring the importance of early COPD screening to prevent the occurrence of COPD and its associated comorbidities.

COPD is a complex and heterogeneous disease. Common methods for establishing COPD mouse model include chronic smoke exposure, CS combined with LPS, LPS combined with PPE, and intraperitoneal CSE at present [30,51,52]. However, no single animal model can replicate all the features of human COPD. Since exposure to cigarette smoke is an independent risk factor for COPD, long-term exposure to cigarette smoke more closely reflects the pathogenesis of the disease in humans and is the most widely accepted modeling method among researchers [34,53]. This model is also commonly used in studies of COPD comorbidities, such as cognitive dysfunction and sarcopenia [54,55]. Indicators of successful COPD mouse model construction included pulmonary histology showing emphysema, airway fibrosis, and increased mucus secretion, pulmonary function indicators such as decreased FEV20/FVC ratio, and increased levels of inflammation in serum and alveolar lavage fluid [56]. In our study, we chose the well-known long-term CS exposure for 24 weeks to establish an animal model and simultaneously evaluate pulmonary and cognitive functions. Long-term CS exposure for 24 weeks is more consistent with the characteristics observed in patients with COPD. We demonstrated the validity and stability of this COPD mouse model at the lung pathology level.

Few studies have investigated cognitive function in animal models of COPD. Charlotte E. Pelgrim also found brain-related damage in a COPD mouse model constructed using lipopolysaccharide combined with elastase, including cognitive dysfunction, decreased motor and blood–brain barrier integrity, and changes in brain kynurenine pathway markers [41]. Numerous studies have indicated that patients with COPD experience deficits in attention, memory, learning capacity, and motor function [57,58], with 62 % of patients with COPD exhibiting short-term

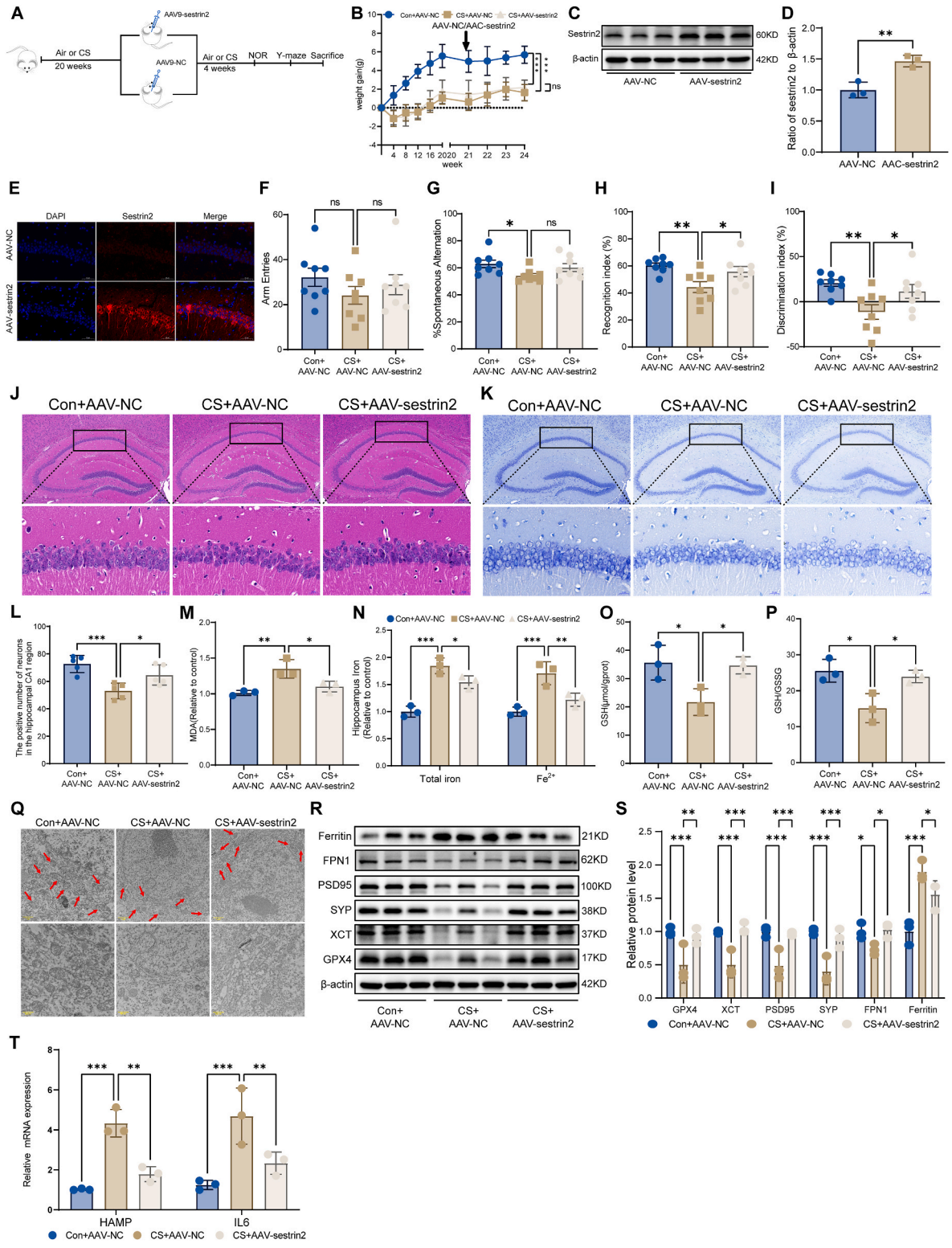

Fig. 12. AAV-mediated sestrin2 overexpression attenuates CS-induced cognitive deficits.
(A)Illustration of the experimental timeline. (B) Mean body weight gain in each group during the 24 weeks(n = 8). (C–D) The protein levels of sestrin2 in the hippocampus were confirmed by Western blot at four weeks after injection. (E) Representative immunofluorescence image of sestrin2 in CA1 neurons was detected 4 weeks after injection. (F) Arm entries in the Y Maze(n = 8). (G) Percentage spontaneous alternation in Y Maze(n = 8). (H) Recognition index (%) in the NOR test(n = 8). (I) Discrimination index (%) in the NOR test(n = 8). (J) HE staining of hippocampus tissue of mice (n = 5) (scale bar = 20 μm). (K) Nissl staining of pulmonary tissue of mice (n = 5) (scale bar = 20 μm). (L) Quantitative analysis of Nissl body positive cells in the CA1 region. (M) MDA levels of the hippocampus in each group. (N) Total iron and Fe^{2+} levels of the hippocampus in each group. (O) GSH levels of the hippocampus in each group. (P) GSH/GSSG ratio of the hippocampus in each group. (Q) Representative TEM images in the hippocampus of each group. (R–S) Western blot and semiquantitative analysis of PSD95, SYP, XCT, GPX4, FPN1 and Ferritin in the hippocampus of each group. (T) RT-qPCR detection of HAMP and IL6 mRNA in the hippocampus of each group. $^{*}P < 0.05$, $^{**}P < 0.01$, $^{***}P < 0.001$.

memory deficits [59]. We also demonstrated that COPD mice have impaired working and spatial memory. Several studies have confirmed a strong association between the CA1 region and the formation of working memory. Recent studies have also found that decreased remapping ability of the hippocampal CA1 region is an essential mechanism for the decline in spatial memory ability in the elderly [60], and the ventral subiculum also plays a key role in spatial learning and memory [61], echoing our clinical findings. We also observed morphological and histological changes in the hippocampus of COPD mice, such as neuronal loss and decreased synaptic protein levels, consistent with a previous study [11,54].

We also established an animal model of COPD by LPS combined with PPE, a nicotine-free modeling method, and evaluated lung and cognitive function at the same time. The results confirmed that mainly affected the working memory of mice and had little effect on spatial memory, which was similar with previous study [41]. While some cognitive changes may be attributed to nicotine, there are studies that have shown that nicotine-free e-cigarettes have impaired novel object recognition performance [62]. In addition to nicotine, many chemicals and free radicals have been identified in cigarettes, including ROS and reactive nitrogen species (RNS) [63], which are also involved in the damage process. In addition, nicotine effects gradually subsided after smoking cessation, but cognitive function improvements in COPD were limited, and oxidative stress in the hippocampus persisted [54]. The impaired cognitive function in COPD is the result of the combination of the disease itself and the systemic effects of nicotine, which is consistent with the previous study [64]. However, the molecular mechanisms underlying COPD-related cognitive dysfunction remain unclear.Common mechanisms include systemic inflammation and oxidative stress, hypoxemia, hypercapnia, and cigarette. Chronic hypoxia, as a clinical feature of COPD, may partially explain the occurrence of cognitive dysfunction in COPD. However, increasing evidence suggests that hypoxemia may not be the primary factor leading to cognitive impairment. Research has found that compared to healthy controls, COPD patients without hypoxemia also exhibit poorer cognitive function [65]. Additionally, neuroimaging findings reveal hippocampal atrophy in COPD patients even in the absence of hypoxemia, accompanied by marked reductions in white matter integrity and diminished gray matter functional activation [66]. This suggests that hypoxemia is not the only cause of cognitive dysfunction in COPD patients. These COPD patients without hypoxemia often have other factors, such as smoking and inflammation, that may affect brain function. Therefore, this motivates us to further explore the mechanisms underlying cognitive dysfunction in COPD beyond hypoxia, providing a scientific basis for the prevention and treatment of COPD-related cognitive dysfunction.

Oxidative stress is a key trigger of CS-induced cognitive dysfunction [67]. De Luca et al. [54] found that increased levels of lipid peroxidation were associated with cognitive impairment in the hippocampus of CS-exposed mice. The excessive accumulation of lipid peroxidation is the most important cause of ferroptosis. However, literature on the effects of CS-induced ferroptosis in the brain is limited. The TEM results revealed an obvious accumulation of shrunken mitochondria in vivo and in vitro. XCT-GPX4, a prominent oxidative stress-related pathway in ferroptosis, was inhibited by CS exposure. Considering that apoptosis and necroptosis are involved in COPD, our study further confirmed that Fer-1 significantly attenuates CSE-induced cell death in hippocampal neurons, suggesting that CSE-induced cell death depends on ferroptosis, which is consistent with the results of a previous study [21,24]. Necroptosis inhibitors reduced CSE-induced cell death at 24h. Previous study found that ferroptosis appears to be the first cell death pathway activated in folic acid-induced acute kidney injury, promoting inflammatory responses and acting as a driver of other forms of cell death, including apoptosis and necroptosis [68]. In addition, ferroptosis inhibitors significantly alleviate CSE-induced lipid peroxidation, mitochondrial destruction, and synaptic protein damage in hippocampal neurons. Consequently, ferroptosis may play a crucial role in COPD-related cognitive impairment.

To further identify the regulatory mechanism of ferroptosis in COPD-related cognitive impairment, we found that sestrin2 may be a key ferroptosis-related gene involved in cognitive impairment. Previous reports found a significant increase in sestrin2 protein levels in the lung tissue of CS-exposed mice [69]. Heidler [70] conducted a study of sestrin2 knockout mice in which they were exposed to CS and showed that sestrin2 inactivation protected animals from developing CS-induced emphysema. To the best of our knowledge, the present study is the first to report that sestrin2 expression is significantly elevated in the hippocampal tissue of mice exposed to CS, as well as in HT22 cells treated with CSE. Based on the antioxidant function of sestrin2 and its association with protection against mitochondrial homeostasis, sestrin2 has been noted to regulate ferroptosis. Currently, sestrin2 has been confirmed to regulate the occurrence of ferroptosis in various diseases, such as diabetic retinopathy, sepsis, and cerebral ischemia-reperfusion injury. Consistent with previous studies [26,27], we found that CSE induces XCT/GPX4 reduction, cell death, lipid peroxidation, MDA formation, and GSH depletion. Sestrin2 overexpression inhibits ferroptosis characteristics, whereas sestrin2 downregulation intensified ferroptosis by reducing its antioxidative capacity.

The mechanism by which sestrin2 regulates ferroptosis was examined. As previously reported, sestrin2 does not directly interact with the XCT/GPX4 [27]. Sestrin2 was confirmed to alleviate ferroptosis caused by intestinal ischemia-reperfusion injury by activating the Keap1/Nrf2 signaling pathway [27]. Li et al. [26] found that sestrin2 could inhibit the ferroptosis of dendritic cells in sepsis by inhibiting the ATF4-CHOP-CHAC1 signaling pathway. In this study, we demonstrated for the first time that sestrin2 can bind to HNRNPL and play a role in inhibiting ferroptosis. Heterogeneous ribonucleoproteins (hnRNPs) represent a diverse group of RNA-binding proteins, with HNRNPL being a key component of the nuclear hnRNP complex [71]. Predominantly localized in the nucleus, HNRNPL plays a critical role in the regulation of mRNA synthesis, transport, and processing [72–75]. Yang et al. [76] found that HNRNPL promoted ferroptosis in hepatocellular carcinoma cells by promoting S100A9 expression. Liu et al. [77] found that HNRNPL may be a major factor in the pathogenesis of smoke-induced hemifacial microsomia pathogenesis. Consistent with the results of bioinformatics analysis, we found that HNRNPL and sestrin2 showed opposite trends in cell and animal models of CS intervention, suggesting that CS intervention may break the balance of the sestrin2-HNRNPL complex. At the same time, siHNRNPL blocked the protective effect of sestrin2 on ferroptosis. These results revealed that the protective effects of sestrin2 are co-mediated by binding to HNRNPL. Aiming to clarify the relationship between sestrin2/HNRNPL and ferroptosis, the results of actinomycin D assays showed that sestrin2 overexpression increased the stability of GPX4 and XCT mRNA, whereas HNRNPL knockdown significantly reduced their stability and abolished the protective effect of sestrin2. These findings indicate that the sestrin2/HNRNPL protects cells from ferroptosis by maintaining GPX4 and XCT mRNA stability and expression. Additionally, HNRNPL is involved in pre-mRNA alternative splicing by specifically binding to pre-mRNA to form complexes or competitively interacting with splice sites, thereby blocking the binding of other splicing factors. Abnormal mRNA splicing is implicated in disease pathogenesis [78]. Whether HNRNPL influences ferroptosis through alternative splicing remains an open question for future investigation.

Iron metabolism imbalance is one of the key mechanisms of ferroptosis. Previous studies have confirmed that CSE can promote ferroptosis by inducing ferritinophagy in airway epithelial cells and skeletal muscle cells [21,24]. How sestrin2 affects iron metabolism is not yet clear. In this study, we found that the expression of HAMP, ferritin and IL6 increased after CS stimulation, while the expression of FPN1 decreased, and this change was reversed after overexpression of sestrin2 and aggravated after knockdown of HNRNPL. FPN1 is a key cellular iron efflux protein. Previous studies have confirmed that hepcidin can bind to

FPN1. When hepcidin binds to FPN1, FPN1 is degraded and lost its function of efflux iron [79]. Recent studies have found that cigarette tar can induce the up-regulation of hepcidin in macrophages, which leads to the degradation of FPN1 and abnormal intracellular iron efflux function, eventually leading to iron overload in macrophages and ferroptosis, thus promoting the progression of atherosclerosis [80]. IL6 is a common inflammatory factor in COPD systemic inflammation, and circulating IL6 levels are associated with cognitive dysfunction. In the inflammatory situation, IL6 promotes hepcidin production through the JAK/STAT3 pathway [80]. We also detected elevated levels of IL6 in all three groups. Therefore, we hypothesized that in COPD patients, circulating IL-6 impairs the integrity of endothelial cells in the blood-brain barrier, allowing innate immune cells in the blood, toxic substances in cigarette, and circulating IL-6 to cross the blood-brain barrier and enter the brain tissue. Together, they promote the increase in the expression of hepcidin, which leads to the degradation of FPN1. The reduction of iron efflux in neurons leads to intracellular iron overload, accompanied by the production of a large number of reactive oxygen species, and finally leads to ferroptosis of neurons. It was also found that astrocyte derived hepcidin controls iron transport in the blood-brain barrier by regulating FPN1 of microvascular endothelial cells [81]. This mechanism deserves further exploration in the future, which is an innovative supplement to the pathogenesis of hippocampal ferroptosis in COPD, providing a new theoretical basis for systemic symptoms of COPD, and is worthy of in-depth study in the future.

At the clinical level, we found elevated serum ferritin and hepcidin in patients with COPD. COPD, as a systemic inflammatory disease, is in a state of systemic low-grade inflammation. Chronic inflammation can stimulate the synthesis of ferritin and the disorder of iron metabolism, and enhanced oxidative stress can also stimulate the increase of ferritin, indicating abnormal iron distribution in COPD patients [82]. The serum iron and Fe^{2+} content decreased in COPD patients, which was considered to be related to the increase of hepcidin. In the state of chronic inflammation, increased hepcidin reduces the uptake of iron by intestinal epithelial cells and blocks the release of iron from cells [83], which is also one of the reasons why COPD patients are often complicated with chronic anemia. We also intervened with the iron chelator DFO in vivo and in vitro experiments. DFO caused a significant improvement in cognitive functions. These results suggest that targeting ferroptosis may be an innovative new strategy for the treatment of COPD and warrants further investigation in the future.

Only a few in vivo experiments have so far been conducted on the regulation of cognitive function by sestrin2. Sun L found that the overexpression of sestrin2 improved sevoflurane-induced cognitive dysfunction and inhibited the generation of apoptosis in hippocampal neurons [84]. In this study, we found that after overexpression of sestrin2, COPD mice achieved partial improvement in the Y-maze, albeit not significant, while the NOR results were significantly improved. This suggests that the neuroprotective effect of sestrin2 overexpression is mainly manifested in the recovery of working memory in COPD mice. At the same time, considering that COPD mice are older and have poor cardiopulmonary function, we only performed unilateral AAV injection to ensure the survival rate of mice after injection, which may also be one of the reasons. In addition, hippocampal ferroptosis was significantly inhibited, and synaptic damage was alleviated after sestrin2 overexpression. Previous studies have found that GPX4 overexpression can improve memory impairment in mice [85], which also initially explains that sestrin2 may affect ferroptosis through GPX4 to alleviate cognitive impairment.

Redox imbalance is recognized as a central mechanism underlying the pathogenesis of COPD and its extra-pulmonary comorbidities. However, comprehensive studies integrating both clinical and experimental data to elucidate its role in COPD-related cognitive dysfunction remain lacking. Ferroptosis, a recently characterized form of regulated cell death driven by redox dysregulation, has been predominantly investigated in pulmonary tissues of COPD models. Exploring ferroptosis within the hippocampus may provide critical insights into the contribution of redox imbalance to COPD-associated neurocognitive decline. This study, for the first time, comprehensively confirms that sestrin2 alleviates cognitive impairment via inhibiting hippocampus ferroptosis in cigarette smoke-induced chronic obstructive pulmonary disease at the clinical, animal, and cellular levels. It helps in bridging the gap in understanding the interplay between neurodegeneration and systemic diseases like COPD. Such approaches may overcome the limitations of conventional antioxidant therapies and offer a new conceptual framework for addressing the systemic effects of chronic inflammatory diseases.

Our study has some limitations. First, given the experimental conditions, we did not explore the relationship between serum sestrin2 expression and cognitive function in patients with COPD. Second, we initially confirmed that the Sestrin2-HNRNPL complex jointly regulates the occurrence of ferroptosis, and the specific binding sites or intrinsic regulatory mechanisms of sestrin2 and HNRNPL are worth further exploration. Third, there are few studies on the molecular mechanism of cognitive dysfunction in COPD. We selected CSE stimulated HT22 cells for our in vitro experiment referring to previous study. The primary hippocampal neurons of COPD mice will better reflect the pathological mechanism of COPD cognitive dysfunction. Fourth, due to the difficulty in obtaining human brain specimens, quantitative magnetic susceptibility imaging (QSM) is currently an emerging magnetic resonance imaging technique that can detect iron deposition in the brain. Fe concentration in mouse hippocampus could be measured using inductively coupled plasma mass spectrometry. Although currently limited by technical conditions, we lack this part of quantitative data at present. Subsequently, we will further detect and compare iron deposition in the hippocampus of COPD patients through QSM, and dynamically monitor the changes in iron content in the hippocampus of mice during CS exposure through more quantitative methods.

5. Conclusions

Significant atrophy of hippocampal volume was observed with the most pronounced alterations occurring in the CA1 region in patients with COPD. CS exposure damaged neurons in the hippocampus and caused cognitive dysfunction. Ferroptosis is a potential key mechanism of CS-induced neuronal injury. Increased expression of sestrin2 induced by cigarettes was found in CS-exposed mice and hippocampal neuronal cell HT22. Moreover, sestrin2 overexpression could prevent CS-induced cognitive dysfunction by reducing the occurrence of ferroptosis directly bound to HNRNPL. This study developed a novel insight into the possible mechanisms involved in cognitive dysfunction in COPD, and sestrin2 could be a potential therapeutic target for COPD-related cognitive dysfunction.

CRediT authorship contribution statement

Da-Wei Zhang: Writing – original draft, Validation, Investigation, Formal analysis, Conceptualization. **Ming-Ming Yang:** Methodology, Investigation, Data curation. **Meng-Xi Zhou:** Software, Investigation, Formal analysis. **Yuan-Yuan Wei:** Supervision, Investigation. **Lei Hu:** Visualization, Investigation. **Mei Hong:** Investigation. **Ting-Ting Chen:** Investigation. **Xiao-Min Wang:** Investigation. **Yi-Chuan Ding:** Investigation. **Chuan-Sheng Wei:** Investigation. **Fang Li:** Investigation. **Wen Chen:** Investigation. **Jia-Ying Kang:** Formal analysis. **Jing-Jing Ye:** Formal analysis. **Guang-He Fei:** Writing – review & editing, Funding acquisition, Conceptualization.

Ethics approval and consent to participate

All animal experiments were approved by the Institutional Animal Care and Use Committee of Anhui Medical University (Ethics No. LLSC20242226). All human experiments were was approved by the

ethical committee of Anhui Medical University (Ethics No. PJ2024-07-58).

Data availability statement

Data will be made available on reasonable request.

Funding

This work was supported by the National Natural Science Foundation of China (No.82170050, 82470034), Anhui Province clinical medical research transformation project (No.202304295107020038), Anhui university excellent research and innovation team plan (No.2023AH010082).

Declaration of competing interest

The authors declare that they have no known competing financial interests or personal relationships that could have appeared to influence the work reported in this paper.

Acknowledgements

We thank for the support of Center for Scientific Research, Anhui Medical University. We thank BioRender (https://www.biorender.com/) for assisting in drawing graphical abstract. We thank LetPub (https://www.letpub.com) for its linguistic assistance during the preparation of this manuscript.

Abbreviations

COPD	chronic obstructive pulmonary disease
CS	cigarette smoke
ROS	Reactive oxygen species
CSE	cigarette smoke extract
AAV	adeno-associated viral
HNRNPL	heterogeneous nuclear ribonucleoprotein L
MRI	magnetic resonance imaging
3D	three-dimensional
TR	repetition time
TE	echo time
eTIV	estimated total intracranial volume
FVC	forced vital capacity
FEV20	forced expiratory volume in 20 ms
BALF	bronchoalveolar lavage fluid
HE	hematoxylin/eosin
AB-PAS	alcian blue-periodic acid schiff
PBS	phosphate-buffered saline
ELISA	enzyme-linked immunosorbent assay
NOR	novel target recognition
WB	western blot
qRT-PCR	quantitative real-time polymerase chain reaction
CCK-8	cell counting kit-8
TEM	transmission electron microscopy
MDA	malondialdehyde
MMP	Mitochondrial membrane potential
GSH	glutathione
IF	immunofluorescence
Co-IP	coimmunoprecipitation
SYP	synaptophysin
Fer-1	ferrostatin-1; hnRNPs: heterogeneous ribonucleoproteins
RNS	reactive nitrogen species
DEG	differentially expressed genes
QSM	quantitative magnetic susceptibility imaging

Appendix A. Supplementary data

Supplementary data to this article can be found online at https://doi.org/10.1016/j.redox.2025.103673.

Data availability

Data will be made available on request.

References

[1] A. Agustí, B.R. Celli, G.J. Criner, D. Halpin, A. Anzueto, P. Barnes, J. Bourbeau, M. K. Han, F.J. Martinez, M. Montes de Oca, K. Mortimer, A. Papi, I. Pavord, N. Roche, S. Salvi, D.D. Sin, D. Singh, R. Stockley, M.V. López Varela, J.A. Wedzicha, C. F. Vogelmeier, Global Initiative for chronic obstructive lung disease 2023 report: GOLD executive summary, Eur. Respir. J. 61 (4) (2023).
[2] L.C. Oostwoud, P. Gunasinghe, H.J. Seow, J.M. Ye, S. Selemidis, S. Bozinovski, R. Vlahos, Apocynin and ebselen reduce influenza A virus-induced lung inflammation in cigarette smoke-exposed mice, Sci. Rep. 6 (2016) 20983.
[3] E.E. Yazar, S. Aydin, G. Gunluoglu, S. Kamat, A.C. Gungen, P. Yildiz, Clinical effects of cognitive impairment in patients with chronic obstructive pulmonary disease, Chron. Respir. Dis. 15 (3) (2018) 306–314.
[4] M.E.D.A. Shehata, H.M.S. Samaha, A.R. Elsaid, E.M. Helmy, W. Mustafa, Magnetic resonance apparent diffusion coefficient values of the brain in COPD, Egypt. J. Chest Dis. Tuberc. 66 (2) (2017) 237–242.
[5] J.W. Dodd, S.V. Getov, P.W. Jones, Cognitive function in COPD, Eur. Respir. J. 35 (4) (2010) 913–922.
[6] J.W. Dodd, R.A. Charlton, M.D. van den Broek, P.W. Jones, Cognitive dysfunction in patients hospitalized with acute exacerbation of COPD, Chest 144 (1) (2013) 119–127.
[7] R. Antonelli-Incalzi, A. Corsonello, C. Pedone, L. Trojano, D. Acanfora, A. Spada, O. Izzo, F. Rengo, Drawing impairment predicts mortality in severe COPD, Chest 130 (6) (2006) 1687–1694.
[8] X. Wang, E.K. Michaelis, Selective neuronal vulnerability to oxidative stress in the brain, Front. Aging Neurosci. 2 (2010) 12.
[9] J. Li, G.H. Fei, The unique alterations of hippocampus and cognitive impairment in chronic obstructive pulmonary disease, Respiratory research 14 (1) (2013) 140.
[10] G. Caramori, P. Casolari, A. Barczyk, A.L. Durham, A. Di Stefano, I. Adcock, COPD immunopathology, Semin. Immunopathol. 38 (4) (2016) 497–515.
[11] A. Dobric, S.N. De Luca, H.J. Seow, H. Wang, K. Brassington, S.M.H. Chan, K. Mou, J. Erlich, S. Liong, S. Selemidis, S.J. Spencer, S. Bozinovski, R. Vlahos, Cigarette smoke exposure induces neurocognitive impairments and neuropathological changes in the Hippocampus, Front. Mol. Neurosci. 15 (2022) 893083.
[12] L. Zhao, T. Chen, C. Wang, G. Li, W. Zhi, J. Yin, Q. Wan, L. Chen, Atorvastatin in improvement of cognitive impairments caused by amyloid β in mice: involvement of inflammatory reaction, BMC Neurol. 16 (2016) 18.
[13] A.C. Sartori, D.E. Vance, L.Z. Slater, M. Crowe, The impact of inflammation on cognitive function in older adults: implications for healthcare practice and research, J. Neurosci. Nurs. : journal of the American Association of Neuroscience Nurses 44 (4) (2012) 206–217.
[14] C.E. Pelgrim, L. Wang, L.N. Peralta Marzal, S. Korver, I. van Ark, T. Leusink-Muis, S. Braber, G. Folkerts, J. Garssen, A. van Helvoort, A.D. Kraneveld, Increased exploration and hyperlocomotion in a cigarette smoke and LPS-induced murine model of COPD: linking pulmonary and systemic inflammation with the brain, American journal of physiology, Lung cellular and molecular physiology 323 (3) (2022) L251–l265.
[15] R. Dantzer, J.C. O'Connor, G.G. Freund, R.W. Johnson, K.W. Kelley, From inflammation to sickness and depression: when the immune system subjugates the brain, Nat. Rev. Neurosci. 9 (1) (2008) 46–56.
[16] X. Yang, A.L. Guo, Y.P. Pang, X.J. Cheng, T. Xu, X.R. Li, J. Liu, Y.Y. Zhang, Y. Liu, Astaxanthin attenuates environmental tobacco smoke-induced cognitive deficits: a critical role of p38 mapk, Mar. Drugs 17 (1) (2019).
[17] D.J. DiSabato, N. Quan, J.P. Godbout, Neuroinflammation: the devil is in the details, J. Neurochem. 139 (Suppl 2) (2016) 136–153.
[18] B. Singh, M.M. Mielke, A.K. Parsaik, R.H. Cha, R.O. Roberts, P.D. Scanlon, Y. E. Geda, T.J. Christianson, V.S. Pankratz, R.C. Petersen, A prospective study of chronic obstructive pulmonary disease and the risk for mild cognitive impairment, JAMA Neurol. 71 (5) (2014) 581–588.
[19] I. Torres-Sánchez, E. Rodríguez-Alzueta, I. Cabrera-Martos, I. López-Torres, M. P. Moreno-Ramírez, M.C. Valenza, Cognitive impairment in COPD: a systematic review, J. Bras. Pneumol. : publicacao oficial da Sociedade Brasileira de Pneumologia e Tisilogia 41 (2) (2015) 182–190.
[20] B.R. Stockwell, Ferroptosis turns 10: emerging mechanisms, physiological functions, and therapeutic applications, Cell 185 (14) (2022) 2401–2421.
[21] M. Yoshida, S. Minagawa, J. Araya, T. Sakamoto, H. Hara, K. Tsubouchi, Y. Hosaka, A. Ichikawa, N. Saito, T. Kadota, N. Sato, Y. Kurita, K. Kobayashi, S. Ito, H. Utsumi, H. Wakui, T. Numata, Y. Kaneko, S. Mori, H. Asano, M. Yamashita, M. Odaka, T. Morikawa, K. Nakayama, T. Iwamoto, H. Imai, K. Kuwano, Involvement of cigarette smoke-induced epithelial cell ferroptosis in COPD pathogenesis, Nat. Commun. 10 (1) (2019) 3145.
[22] T.C. Durazzo, N. Mattsson, M.W. Weiner, Smoking and increased Alzheimer's disease risk: a review of potential mechanisms, Alzheimer's & dementia : the journal of the Alzheimer's Association 10 (3 Suppl) (2014) S122–S145.

[23] R. Tian, A. Abarientos, J. Hong, S.H. Hashemi, R. Yan, N. Dräger, K. Leng, M. A. Nalls, A.B. Singleton, K. Xu, F. Faghri, M. Kampmann, Genome-wide CRISPRi/a screens in human neurons link lysosomal failure to ferroptosis, Nat. Neurosci. 24 (7) (2021) 1020–1034.
[24] Z. Jing, Y. Li, H. Zhang, T. Chen, J. Yu, X. Xu, Y. Zou, X. Wang, K. Xiang, X. Gong, P. He, Y. Fu, M. Ren, P. Ji, S. Yang, Tobacco toxins induce osteoporosis through ferroptosis, Redox Biol. 67 (2023) 102922.
[25] J.H. Lee, A.V. Budanov, E.J. Park, R. Birse, T.E. Kim, G.A. Perkins, K. Ocorr, M. H. Ellisman, R. Bodmer, E. Bier, M. Karin, Sestrin as a feedback inhibitor of TOR that prevents age-related pathologies, Science (New York, N.Y.) 327 (5970) (2010) 1223–1228.
[26] J.Y. Li, C. Ren, L.X. Wang, R.Q. Yao, N. Dong, Y. Wu, Y.P. Tian, Y.M. Yao, Sestrin2 protects dendrite cells against ferroptosis induced by sepsis, Cell Death Dis. 12 (9) (2021) 834.
[27] L.L. Zhang, K. Ding, S.S. Liao, Y.G. Zhang, H.Y. Liao, R. Chen, Q.T. Meng, Sestrin2 reduces ferroptosis via the Keap1/Nrf2 signaling pathway after intestinal ischemia-reperfusion, Free radical biology & medicine 214 (2024) 115–128.
[28] D.W. Zhang, Y.Y. Wei, S. Ji, G.H. Fei, Correlation between sestrin2 expression and airway remodeling in COPD, BMC Pulm. Med. 20 (1) (2020) 297.
[29] S. Takahashi, T. Hirano, K. Yasuda, T. Donishi, K. Suga, K. Doi, K. Oishi, S. Ohata, Y. Murata, Y. Yamaji, M. Asami-Noyama, N. Edakuni, K. Matsunaga, Impact of frailty on hippocampal volume in patients with chronic obstructive pulmonary disease, Biomedicines 9 (9) (2021).
[30] Z. Yan, B. Chen, Y. Yang, X. Yi, M. Wei, G. Ecklu-Mensah, M.M. Buschmann, H. Liu, J. Gao, W. Liang, X. Liu, J. Yang, W. Ma, Z. Liang, F. Wang, D. Chen, L. Wang, W. Shi, M.R. Stampfli, P. Li, S. Gong, X. Chen, W. Shu, E.M. El-Omar, J.A. Gilbert, M.J. Blaser, H. Zhou, R. Chen, Z. Wang, Multi-omics analyses of airway host-microbe interactions in chronic obstructive pulmonary disease identify potential therapeutic interventions, Nat. Microbiol. 7 (9) (2022) 1361–1375.
[31] J.Y. Kang, M.M. Xu, Y. Sun, Z.X. Ding, Y.Y. Wei, D.W. Zhang, Y.G. Wang, J.L. Shen, H.M. Wu, G.H. Fei, Melatonin attenuates LPS-induced pyroptosis in acute lung injury by inhibiting NLRP3-GSDMD pathway via activating Nrf2/HO-1 signaling axis, Int. Immunopharmacol. 109 (2022) 108782.
[32] T.T. Chen, Y.Y. Wei, J.Y. Kang, D.W. Zhang, J.J. Ye, X.S. Sun, M. Hong, W. T. Zhang, H.M. Wu, Z.X. Ding, G.H. Fei, ADAR1-HNRNPL-Mediated CircCANX decline promotes autophagy in chronic obstructive pulmonary disease, Advanced science (Weinheim, Baden-Wurttemberg, Germany) (2025) e2414211.
[33] M.M. Xu, J.Y. Kang, Q.Y. Wang, X. Zuo, Y.Y. Tan, Y.Y. Wei, D.W. Zhang, L. Zhang, H.M. Wu, G.H. Fei, Melatonin improves influenza virus infection-induced acute exacerbation of COPD by suppressing macrophage M1 polarization and apoptosis, Respiratory research 25 (1) (2024) 186.
[34] Z. Zeng, T. Li, X. Liu, Y. Ma, L. Luo, Z. Wang, Z. Zhao, H. Li, X. He, H. Zeng, Y. Tao, Y. Chen, DNA dioxygenases TET2 deficiency promotes cigarette smoke induced chronic obstructive pulmonary disease by inducing ferroptosis of lung epithelial cell, Redox Biol. 67 (2023) 102916.
[35] T. Barrett, S.E. Wilhite, P. Ledoux, C. Evangelista, I.F. Kim, M. Tomashevsky, K. A. Marshall, K.H. Phillippy, P.M. Sherman, M. Holko, A. Yefanov, H. Lee, N. Zhang, C.L. Robertson, N. Serova, S. Davis, A. Soboleva, NCBI GEO: archive for functional genomics data sets–update, Nucleic acids research 41 (Database issue) (2013) D991–D995.
[36] W.S. Liang, T. Dunckley, T.G. Beach, A. Grover, D. Mastroeni, D.G. Walker, R. J. Caselli, W.A. Kukull, D. McKeel, J.C. Morris, C. Hulette, D. Schmechel, G. E. Alexander, E.M. Reiman, J. Rogers, D.A. Stephan, Gene expression profiles in anatomically and functionally distinct regions of the normal aged human brain, Physiol. Genom. 28 (3) (2007) 311–322.
[37] E.M. Blalock, H.M. Buechel, J. Popovic, J.W. Geddes, P.W. Landfield, Microarray analyses of laser-captured hippocampus reveal distinct gray and white matter signatures associated with incipient Alzheimer's disease, J. Chem. Neuroanat. 42 (2) (2011) 118–126.
[38] M.E. Ritchie, B. Phipson, D. Wu, Y. Hu, C.W. Law, W. Shi, G.K. Smyth, Limma powers differential expression analyses for RNA-sequencing and microarray studies, Nucleic acids research 43 (7) (2015) e47.
[39] N. Zhou, J. Bao, FerrDb: a Manually Curated Resource for Regulators and Markers of Ferroptosis and Ferroptosis-Disease Associations, Database : the Journal of Biological Databases and Curation 2020, 2020.
[40] Z. Tang, C. Li, B. Kang, G. Gao, C. Li, Z. Zhang, GEPIA: a web server for cancer and normal gene expression profiling and interactive analyses, Nucleic acids research 45 (W1) (2017) W98–W102.
[41] C.E. Pelgrim, I. van Ark, R.E. van Berkum, A.M. Schuitemaker-Borneman, I. Flier, T. Leusink-Muis, H. Janbazacyabar, M.A.P. Diks, H.R. Gosker, M. Kelders, R.C. J. Langen, A. Schols, R.J.J. Hageman, S. Braber, J. Garssen, G. Folkerts, A. van Helvoort, A.D. Kraneveld, Effects of a nutritional intervention on impaired behavior and cognitive function in an emphysematous murine model of COPD with endotoxin-induced lung inflammation, Front. Nutr. 9 (2022) 1010989.
[42] A.J. Fix, D. Daughton, I. Kass, C.W. Bell, C.J. Golden, Cognitive functioning and survival among patients with chronic obstructive pulmonary disease, Int. J. Neurosci. 27 (1–2) (1985) 13–17.
[43] L.G. Apostolova, A.E. Green, S. Babakchanian, K.S. Hwang, Y.Y. Chou, A.W. Toga, P.M. Thompson, Hippocampal atrophy and ventricular enlargement in normal aging, mild cognitive impairment (MCI), and Alzheimer Disease, Alzheimer disease and associated disorders 26 (1) (2012) 17–27.
[44] L.G. Apostolova, J.H. Morra, A.E. Green, K.S. Hwang, C. Avedissian, E. Woo, J. L. Cummings, A.W. Toga, C.R. Jack Jr., M.W. Weiner, P.M. Thompson, Automated 3D mapping of baseline and 12-month associations between three verbal memory measures and hippocampal atrophy in 490 ADNI subjects, Neuroimage 51 (1) (2010) 488–499.
[45] R.W. Esser, M.C. Stoeckel, A. Kirsten, H. Watz, K. Taube, K. Lehmann, S. Petersen, H. Magnussen, A. von Leupoldt, Structural brain changes in patients with COPD, Chest 149 (2) (2016) 426–434.
[46] J.L. Daval, G. Pourié, S. Grojean, V. Lièvre, C. Strazielle, S. Blaise, P. Vert, Neonatal hypoxia triggers transient apoptosis followed by neurogenesis in the rat CA1 hippocampus, Pediatr. Res. 55 (4) (2004) 561–567.
[47] T. Kitanishi, R. Umaba, K. Mizuseki, Robust information routing by dorsal subiculum neurons, Sci. Adv. 7 (11) (2021).
[48] J. Chen, I.T. Lin, H. Zhang, J. Lin, S. Zheng, M. Fan, J. Zhang, Reduced cortical thickness, surface area in patients with chronic obstructive pulmonary disease: a surface-based morphometry and neuropsychological study, Brain imaging and behavior 10 (2) (2016) 464–476.
[49] X. Hu, H. Wang, Y. Tu, M. Fei, M. Yin, G. Fei, Y. Yu, Alterations of the default mode network and cognitive impairments in patients with chronic obstructive pulmonary disease, Int. J. Chronic Obstr. Pulm. Dis. 13 (2018) 519–528.
[50] M. Yin, H. Wang, X. Hu, X. Li, G. Fei, Y. Yu, Patterns of brain structural alteration in COPD with different levels of pulmonary function impairment and its association with cognitive deficits, BMC Pulm. Med. 19 (1) (2019) 203.
[51] P. Upadhyay, C.W. Wu, A. Pham, A.A. Zeki, C.M. Royer, U.P. Kodavanti, M. Takeuchi, H. Bayram, K.E. Pinkerton, Animal models and mechanisms of tobacco smoke-induced chronic obstructive pulmonary disease (COPD), Journal of toxicology and environmental health. Part B, Critical reviews 26 (5) (2023) 275–305.
[52] J.L. Wright, M. Cosio, A. Churg, Animal models of chronic obstructive pulmonary disease, American journal of physiology, Lung cellular and molecular physiology 295 (1) (2008) L1–L15.
[53] T.M. Conlon, G. John-Schuster, D. Heide, D. Pfister, M. Lehmann, Y. Hu, Z. Ertüz, M.A. Lopez, M. Ansari, M. Strunz, C. Mayr, I. Angelidis, C. Ciminieri, R. Costa, M. S. Kohlhepp, A. Guillot, G. Günes, A. Jeridi, M.C. Funk, G. Beroshvili, S. Prokosch, J. Hetzer, S.E. Verleden, H. Alsafadi, M. Lindner, G. Burgstaller, L. Becker, M. Irmler, M. Dudek, J. Janzen, E. Goffin, R. Gosens, P. Knolle, B. Pirotte, T. Stoeger, J. Beckers, D. Wagner, I. Singh, F.J. Theis, M.H. de Angelis, T. O'Connor, F. Tacke, M. Boutros, E. Dejardin, O. Eickelberg, H.B. Schiller, M. Königshoff, M. Heikenwalder, A. Yildirim, Inhibition of LTβR signalling activates WNT-induced regeneration in lung, Nature 588 (7836) (2020) 151–156.
[54] S.N. De Luca, K. Brassington, S.M.H. Chan, A. Dobric, K. Mou, H.J. Seow, R. Vlahos, Ebselen prevents cigarette smoke-induced cognitive dysfunction in mice by preserving hippocampal synaptophysin expression, J. Neuroinflammation 19 (1) (2022) 72.
[55] Z. Wang, M. Deng, W. Xu, C. Li, Z. Zheng, J. Li, L. Liao, Q. Zhang, Y. Bian, R. Li, J. Miao, K. Wang, Y. Yin, Y. Li, X. Zhou, G. Hou, DKK3 as a diagnostic marker and potential therapeutic target for sarcopenia in chronic obstructive pulmonary disease, Redox Biol. 78 (2024) 103434.
[56] J.S. Zhou, Z.Y. Li, X.C. Xu, Y. Zhao, Y. Wang, H.P. Chen, M. Zhang, Y.F. Wu, T. W. Lai, C.H. Di, L.L. Dong, J. Liu, N.X. Xuan, C. Zhu, Y.P. Wu, H.Q. Huang, F. G. Yan, W. Hua, Y. Wang, W.N. Xiong, H. Qiu, T. Chen, D. Weng, H.P. Li, X. Zhou, L. Wang, F. Liu, X. Lin, S.M. Ying, W. Li, M. Imamura, M.E. Choi, M.R. Stampfli, A. M.K. Choi, Z.H. Chen, H.H. Shen, Cigarette smoke-initiated autoimmunity facilitates sensitisation to elastin-induced COPD-like pathologies in mice, Eur. Respir. J. 56 (3) (2020).
[57] R. Antonelli-Incalzi, A. Corsonello, L. Trojano, D. Acanfora, A. Spada, O. Izzo, F. Rengo, Correlation between cognitive impairment and dependence in hypoxemic COPD, Journal of clinical and experimental neuropsychology 30 (2) (2008) 141–150.
[58] A.F. Crişan, C. Oancea, B. Timar, O. Fira-Mladinescu, A. Crişan, V. Tudorache, Cognitive impairment in chronic obstructive pulmonary disease, PLoS One 9 (7) (2014) e102468.
[59] B.J. Zarowitz, T. O'Shea, Chronic obstructive pulmonary disease: prevalence, characteristics, and pharmacologic treatment in nursing home residents with cognitive impairment, J. Manag. Care Pharm. : JMCP 18 (8) (2012) 598–606.
[60] L. Zheng, Z. Gao, S. Doner, A. Oyao, M. Forloines, M.D. Grilli, C.A. Barnes, A. D. Ekstrom, Hippocampal contributions to novel spatial learning are both age-related and age-invariant, Proceedings of the National Academy of Sciences of the United States of America 120 (50) (2023) e2307884120.
[61] X.-F. Zhang, Y.-D. Li, Y. Li, Y. Li, D. Xu, L.-L. Bi, H.-B. Xu, Ventral subiculum promotes wakefulness through several pathways in male mice, Neuropsychopharmacology 49 (9) (2024) 1468–1480.
[62] N.A. Heldt, A. Seliga, M. Winfield, S. Gajghate, N. Reichenbach, X. Yu, S. Rom, A. Tenneti, D. May, B.D. Gregory, Y. Persidsky, Electronic cigarette exposure disrupts blood-brain barrier integrity and promotes neuroinflammation, Brain Behav. Immun. 88 (2020) 363–380.
[63] T. Münzel, O. Hahad, M. Kuntic, J.F. Keaney, J.E. Deanfield, A. Daiber, Effects of tobacco cigarettes, e-cigarettes, and waterpipe smoking on endothelial function and clinical outcomes, Eur. Heart J. 41 (41) (2020) 4057–4070.
[64] R. Alateeq, A. Akhtar, S.N. De Luca, S.M.H. Chan, R. Vlahos, Apocynin prevents cigarette smoke-induced anxiety-like behavior and preserves microglial profiles in male mice, Antioxidants 13 (7) (2024).
[65] P.P. Gupta, S. Sood, A. Atreja, D. Agarwal, A comparison of cognitive functions in non-hypoxemic chronic obstructive pulmonary disease (COPD) patients and age-matched healthy volunteers using mini-mental state examination questionnaire and event-related potential, P300 analysis, Lung India, official organ of Indian Chest Society 30 (1) (2013) 5–11.
[66] J.W. Dodd, A.W. Chung, M.D. van den Broek, T.R. Barrick, R.A. Charlton, P. W. Jones, Brain structure and function in chronic obstructive pulmonary disease: a multimodal cranial magnetic resonance imaging study, Am. J. Respir. Crit. Care Med. 186 (3) (2012) 240–245.

[67] A. Kandlur, K. Satyamoorthy, G. Gangadharan, Oxidative stress in cognitive and epigenetic aging: a retrospective glance, Front. Mol. Neurosci. 13 (2020) 41.
[68] D. Martin-Sanchez, J. Poveda, M. Fontecha-Barriuso, O. Ruiz-Andres, M. D. Sanchez-Niño, M. Ruiz-Ortega, A. Ortiz, A.B. Sanz, Targeting of regulated necrosis in kidney disease, Nefrologia 38 (2) (2018) 125–135.
[69] A. Morsch, E. Wisniewski, T.F. Luciano, V.H. Comin, G.B. Silveira, S.O. Marques, A. Thirupathi, P.C. Silveira Lock, C.T. De Souza, Cigarette smoke exposure induces ROS-mediated autophagy by regulating sestrin, AMPK, and mTOR level in mice, Redox Rep. : communications in free radical research 24 (1) (2019) 27–33.
[70] J. Heidler, A. Fysikopoulos, F. Wempe, M. Seimetz, T. Bangsow, A. Tomasovic, F. Veit, S. Scheibe, A. Pichl, F. Weisel, K.C. Lloyd, P. Jaksch, W. Klepetko, N. Weissmann, H. von Melchner, Sestrin-2, a repressor of PDGFRβ signalling, promotes cigarette-smoke-induced pulmonary emphysema in mice and is upregulated in individuals with COPD, Dis. Model. Mech. 6 (6) (2013) 1378–1387.
[71] S. Piñol-Roma, M.S. Swanson, J.G. Gall, G. Dreyfuss, A novel heterogeneous nuclear RNP protein with a unique distribution on nascent transcripts, The Journal of cell biology 109 (6 Pt 1) (1989) 2575–2587.
[72] D.T. Kuninger, T. Izumi, J. Papaconstantinou, S. Mitra, Human AP-endonuclease 1 and hnRNP-L interact with a nCaRE-like repressor element in the AP-endonuclease 1 promoter, Nucleic acids research 30 (3) (2002) 823–829.
[73] P.S. Ray, J. Jia, P. Yao, M. Majumder, M. Hatzoglou, P.L. Fox, A stress-responsive RNA switch regulates VEGFA expression, Nature 457 (7231) (2009) 915–919.
[74] C.R. Rothrock, A.E. House, K.W. Lynch, HnRNP L represses exon splicing via a regulated exonic splicing silencer, The EMBO journal 24 (15) (2005) 2792–2802.
[75] F. Taguchi, H. Kusaba, A. Asai, Y. Iwamoto, K. Yano, H. Nakano, T. Mizukami, N. Saijo, H. Kato, K. Nishio, hnRNP L enhances sensitivity of the cells to KW-2189, Int. J. Cancer 108 (5) (2004) 679–685.
[76] L. Yang, Z. Zhang, X. Yao, X. Wu, Z. Zhang, HNRNPL facilitates ferroptosis in hepatocellular carcinoma cells by promoting S100A9 expression, Transl. Oncol. 43 (2024) 101908.
[77] B. Liu, S. Zhao, L. Ma, T. Zang, C. Huang, X. Tang, Bioinformatics analysis of hub genes involved in smoke-induced hemifacial microsomia pathogenesis, J. Craniofac. Surg. 34 (8) (2023) 2551–2555.
[78] J. Gu, Z. Chen, X. Chen, Z. Wang, Heterogeneous nuclear ribonucleoprotein (hnRNPL) in cancer, Clinica chimica acta; international journal of clinical chemistry 507 (2020) 286–294.
[79] H. Meng, Y. Yu, E. Xie, Q. Wu, X. Yin, B. Zhao, J. Min, F. Wang, Hepatic HDAC3 regulates systemic iron homeostasis and ferroptosis via the hippo signaling pathway, Research 6 (2023) 281.
[80] X. Bao, X. Luo, X. Bai, Y. Lv, X. Weng, S. Zhang, Y. Leng, J. Huang, X. Dai, Y. Wang, J. Li, H. Jia, Cigarette tar mediates macrophage ferroptosis in atherosclerosis through the hepcidin/FPN/SLC7A11 signaling pathway, Free radical biology & medicine 201 (2023) 76–88.
[81] L. You, P.P. Yu, T. Dong, W. Guo, S. Chang, B. Zheng, Y. Ci, F. Wang, P. Yu, G. Gao, Y.Z. Chang, Astrocyte-derived hepcidin controls iron traffic at the blood-brain-barrier via regulating ferroportin 1 of microvascular endothelial cells, Cell Death Dis. 13 (8) (2022) 667.
[82] L. Tandara, T.Z. Grubisic, G. Ivan, Z. Jurisic, M. Tandara, K. Gugo, S. Mladinov, I. Salamunic, Systemic inflammation up-regulates serum hepcidin in exacerbations and stabile chronic obstructive pulmonary disease, Clin. Biochem. 48 (18) (2015) 1252–1257.
[83] D.L. Zhang, T. Senecal, M.C. Ghosh, H. Ollivierre-Wilson, T. Tu, T.A. Rouault, Hepcidin regulates ferroportin expression and intracellular iron homeostasis of erythroblasts, Blood 118 (10) (2011) 2868–2877.
[84] L. Sun, Y. Li, D. Wang, X. Hong, SESN2 attenuates sevoflurane-induced cognitive impairment and neuroinflammation in rats, Exp. Brain Res. 242 (2) (2024) 375–384.
[85] J. Fang, Q. Yuan, Z. Du, Q. Zhang, L. Yang, M. Wang, W. Yang, C. Yuan, J. Yu, G. Wu, J. Hu, Overexpression of GPX4 attenuates cognitive dysfunction through inhibiting hippocampus ferroptosis and neuroinflammation after traumatic brain injury, Free radical biology & medicine 204 (2023) 68–81.